Title

The Seismic Response to Injected Carbon Dioxide: Comparing Observations to Estimates Based Upon Fluid Flow Modeling

Journal

Journal of Geophysical Research: Solid Earth, 124(7)

ISSN

2169-9313

Authors

Vasco, DW
Alfi, Masoud
Hosseini, Seyyed A
et al.

Publication Date

2019-07-01

DOI

10.1029/2018jb016429

Peer reviewed

The Seismic Response to Injected Carbon Dioxide: Comparing Observations to Estimates Based Upon Fluid Flow Modeling

D. W. Vasco[1], Masoud Alfi[2], Seyyed A. Hosseini[3], Rui Zhang[4], Thomas Daley[1], Jonathan B. Ajo-Franklin[1], and Susan D. Hovorka[3]

[1]Energy Geosciences Division, Lawrence Berkeley National Laboratory, Berkeley, CA, United States, [2]Department of Petroleum Engineering, Texas A&M University, College Station, TX, United States, [3]Bureau of Economic Geology, The University of Texas, Austin, TX, United States, [4]School of Geosciences, University of Louisiana at Lafayette, Lafayette, LA, United States

Correspondence to: D. W. Vasco, dwvasco@lbl.gov

Abstract

Time-lapse seismic amplitude differences and travel time shifts, obtained while monitoring enhanced oil recovery at Cranfield, Mississippi, reveal coherent changes that are associated with the injection of carbon dioxide. Rock physics modeling highlights the importance of the oil, brine, and gas content of pore fluids prior to the injection of carbon dioxide. For example, compressional velocity changes due to the injection of carbon dioxide can drop from 300 m/s to less than 100 m/s as the percentage of oil increases from 1% to 50%. Predictions based upon a new technique for modeling wave propagation in a poroelastic medium containing an arbitrary number of fluids, coupled with multicomponent numerical reservoir modeling at Cranfield, reproduce the general pattern of observed seismic amplitude changes and travel time shifts. In particular, time-lapse amplitude changes suggest a significant and widespread lowering of compressional velocities due to the injection of CO_2 into an aquifer bounding the oil rim of the reservoir. It appears that the large-scale variations in preexisting pore fluid content have a major influence on seismic velocity changes, even in the highly heterogeneous reservoir at Cranfield.

1 Introduction

The geological storage of carbon dioxide has been proposed as a means to slow human-induced climate change. Several sites have been devoted to the underground sequestration of carbon dioxide at a variety of scales, from smaller volumes for research purposes as at Ketzin in Germany (Ivanova et al., 2012) and Otway in Australia (Pevzner et al., 2017) to large industrial scale commercial enterprises storing millions of tonnes, such as at Sleipner in Norway (Chadwick et al., 2014; Eiken, 2019) and In Salah in Algeria (Ringrose et al., 2013; Vasco et al., 2018). Currently, economic considerations favor geological storage that is associated with enhanced oil recovery (EOR), involving the injection of carbon dioxide into existing oil and gas reservoirs, such as at the Weyburn CO_2 flood in Canada (White et al., 2011). This approach to carbon capture and storage is likely to increase with

the passage of substantial tax credits linked to the secure geological storage of this greenhouse gas (Edwards & Celia, 2018).

Due to its physical properties and chemical reactivity, the behavior of carbon dioxide can be very different from commonly injected fluids such as water. Thus, the evolution of stored carbon dixoide is an active area of research. Monitoring the movement of injected CO_2 and its impact on subsurface properties contributes to our understanding of its fate upon leaving the well. To date, there have been relatively few published examples of comprehensive seismic monitoring of injected carbon dioxide for either storage or EOR, as compared to other processes such as waterflooding. The most complete and effective seismic monitoring has occurred at the Sleipner field, a carbon storage project in the North Sea (Arts et al., 2008; Boait et al., 2012; Eiken, 2019). Time-lapse seismic monitoring has also proven useful at other sites, such as the In Salah storage project (Gibson-Poole & Raikes, 2010; Zhang et al., 2015) and the EOR project at Weyburn (White et al., 2011; White, 2013a, 2013b), as well as at the Aquistore field site (White et al., 2015). The studies span a diversity of injection strategies and geological environments, from single well injection of a small volume of carbon dioxide, to large-scale projects involving many wells. Most sites consist of sedimentary sequences of sandstones and shales that vary in the degree of lateral heterogeneity and reservoir thickness. However, carbon dixoide EOR is also practiced in carbonate settings, and there have been some comprehensive seismic monitoring programs to determine the effectiveness of the process (Hoversten et al., 2003; Wang et al., 1998) and laboratory experiments to estimate the changes in seismic wave speed as carbon dioxide is introduced (Njiekak et al., 2013).

Heterogeneity is a confounding issue at most sites, and characterization is often inadequate for determining the detailed changes in carbon dioxide saturation both spatially and temporally. At Cranfield, heterogeneity largely takes the form of sand channels and incised conglomerates that are not resolved by seismic, wireline log, or core interpretations (Kordi, 2013). Finally, the entire suite of factors controlling the seismic response to the injection of carbon dioxide in the complicated settings associated with EOR are not always well understood. For example, there are geochemical effects introduced by the carbon dioxide reacting with bonding cements that depend upon the chemical composition and distribution of the cement (Gaus, 2010).

In this paper we reexamine seismic time-lapse monitoring data associated with the injection of large amounts of carbon dioxide at the Cranfield site in Mississippi (Carter et al., 2014; Carter & Spikes, 2013; Ditkof, 2013; Zhang et al., 2013a, 2014), in light of a large-scale multicomponent reservoir simulation (Alfi & Hosseini, 2016; Alfi et al., 2019). This combination of seismic analysis and fluid flow modeling is a follow-on effort to the previous studies by Zhang et al., 2013a (2013a, 2014), (Ditkof, 2013), and *Carter* (Carter & Spikes, 2013; Carter et al., 2014) to see if we can better understand the primary mechanisms responsible for time-lapse changes and

improve our predictions of the location of such changes, possibly reducing discrepancies between modeling results and observations. We extract simple and direct measures from the seismic data, the seismic amplitude changes for reflections from the top of the reservoir and time shifts incurred by seismic waves propagating through the reservoir, and compare them with predictions from the reservoir simulation. Due to the complexities noted above, our main goal is to establish the important factors determining the seismic response. To account for the variability associated with imperfect knowledge of the fluid distribution, we consider simple end-member rock physics models, as well as a more sophisticated multicomponent extension of Biot theory (Biot, 1956a, 1956b), and compare their predictions to the observed changes.

2 Field Geology

2.1 Geologic Setting

The Cranfield reservoir is characterized by a largely circular anticline situated in southwestern Mississippi, the result of underlying salt tectonics. The D-E sandstone unit of the lower Tuscaloosa Formation represents the producing horizon and is the target for the injection of carbon dioxide. The unit consists of incised conglomeratic and sandy channel facies with variable cementation (Kordi, 2013; Lu et al., 2012a). As such, the formation is composed of a fairly heterogeneous distribution of conglomerates, sandstones, and muddy sandstones generated by meandering channels (Lu et al., 2012a), with a thickness that varies between 14 and 26 m. As a result of the anticlinal structure, the top of the reservoir varies in depth between 3,060 and 3,193 m below the ground surface with dips of up to 3°. From well logs it appears that thin mudstone layers separate the conglomerates and sandstones into two to four subunits (Hosseini et al., 2013). However, the lateral extent of the mudstones is unknown, and they do not appear to be field wide. Broadly, the Lower Tuscaloosa is subdivided into a somewhat homogeneous Basal Massive sandstone member that is conformably overlain by the more heterogeneous Stringer sandstone member. The formation is bounded below by a regional unconformity and overlies shales and sandstones of the Washita-Frederickburg Group (Kordi, 2013). It is overlain by the Middle Tuscaloosa, some 60 m of mudstone that forms a pervasive cap over the reservoir.

2.2 Field Structure and Development

The field was discovered in 1943, and the first producing well was completed in 1944 (Alfi & Hosseini, 2016; Alfi et al., 2019). The oil forms a ring around the anticline, below an extensive gas cap. Pressure is maintained by a surrounding aquifer, providing a constant pressure boundary downdip of the hydrocarbons. Over the period of primary production, some 93 wells were active in the field. The reinjection of produced gas from the Tuscaloosa and surrounding formations was used to maintain reservoir pressure (Weaver & Anderson, 1966). However, the reservoir pressure did gradually decline, and

the aquifer encroached upon the oil rim. With increasing water cut the field became too costly to operate, and the gas cap was drawn down and sold, starting in 1960. By 1966 production from the field ended, the wells were plugged, and the field abandoned. Over the intervening decades the aquifer drive from the edges of the field returned the pressure to preproduction levels.

Starting in 2008 Denbury Onshore LLC began an EOR program involving the injection of carbon dioxide from the nearby Jackson Dome (Lu et al., 2012a). Between 2008 and 2015 more than 5 million metric tonnes of newly purchased CO_2 was pumped into the D-E sandstone unit of the lower Tuscaloosa Formation. Injection started with two wells in mid-2008 and increased to 24 wells by 2011 in semi-five-spot patterns with the continuous injection of carbon dioxide. The production wells were designed on a self-lift principle to take advantage of the reservoir pressure increase due to the injection of carbon dioxide (Hosseini et al., 2013). Initial development began at the northern end of the field and proceeded clockwise around the oil ring.

2.3 Reservoir Monitoring

The carbon dioxide EOR project at Cranfield was notable for the comprehensive monitoring effort conducted by over 25 organizations as part of the Department of Energy's Regional Carbon Sequestration Partnerships program (Hovorka et al., 2013). The multiyear program involved linked field measurements and modeling to develop best practices for assessment and monitoring that could be used by future surveillance efforts. Hovorka et al. (2013) describe the extensive hydrological, geophysical, and geochemical techniques that were employed to characterize the behavior and fate of the injected carbon dioxide. Our focus will be on the surface seismic data used to estimate time-lapse changes in the reservoir and on compositional numerical reservoir modeling used to calculate changes in fluid saturations due to production and injection.

2.4 Surface Seismic Observations

Prior to the injection of carbon dioxide, Denbury Onshore contracted a field-wide seismic survey to aid in the subsequent field development. This survey was not designed with time-lapse monitoring in mind. With Department of Energy funding, an initial survey of the northeastern corner of the field was concluded in 2007. A follow-on survey was conducted 3 years later in 2010 over the same portion of the field, a reshoot of the baseline, in an effort to extract time-lapse changes. Both surveys utilized an explosive source with a frequency content from around 5 Hz to over 100 Hz with an amplitude peak in the 25- to 30-Hz range (Ditkof, 2013, p. 48). The baseline survey consisted of a grid of 222 in-lines and 243 cross-lines, for a total of 40,278 traces. The repeat or monitor survey was shot using 222 in-lines and 233 cross-lines. Both surveys had bin spacings of roughly 25 m by 25 m. The shot points were colocated as accurately as possible, using magnetic tags to facilitate reoccupation of the same site. In the interim, between the two surveys, over

two million tons of supercritical carbon dixoide was pumped into the Lower Tuscaloosa Formation.

The two surveys were processed commercially by the contractor GeoTrace using identical workflows and correcting the 2007 survey for static errors in order to match the data from 2010 (Ditkof, 2013; Ditkof et al., 2013). The processing workflow, listed in Ditkof et al. (2013), included refraction and residuals statics, velocity analysis and prestack time migration, and stacking. A matched filter was derived from the baseline data and applied to the monitor survey to enhance the repeatability, resulting in similar average spectral content (Zhang et al., 2013a). Measures of correlation between the 2007 and 2010 surveys, discussed in Ditkof et al. (2013) and Zhang et al. (2013a), indicate high correlations between 0.9 and 1.0 in the central area of the surveys and good repeatability, suggesting useful information on time-lapse changes. The outer edges of the overlapping survey region have much lower correlations and poor repeatability, due to low fold and poor residual statics, and should not be included in any time-lapse analysis (Ditkof, 2013, p. 58).

The reservoir is characterized by a significant decrease in velocity leading to a large negative trough in the seismic traces (Zhang et al., 2013a). Because the reservoir is thin, the top and bottom reflections interfere to some degree. However, it is possible to image spatial variations in the thickness of sandstone bodies that represent channel sands and stacked point bars (Lu et al., 2012a). An analysis of spectral content of the seismic data was used to better define the sandstone accumulations in the reservoir (Kordi, 2013), but the bodies are generally too thin to be resolved uniquely (Lu et al., 2012a). It is possible to identify the top and bottom reflections from the reservoir and to estimate the depth variations of these interfaces with their evident anticlinal structure (Figure 1). Ditkof (2013) compared the estimates of the boundary locations for the 2007 and 2010 surveys and found no significant differences between the two surveys except at a bounding fault where a mismatch may have occurred.

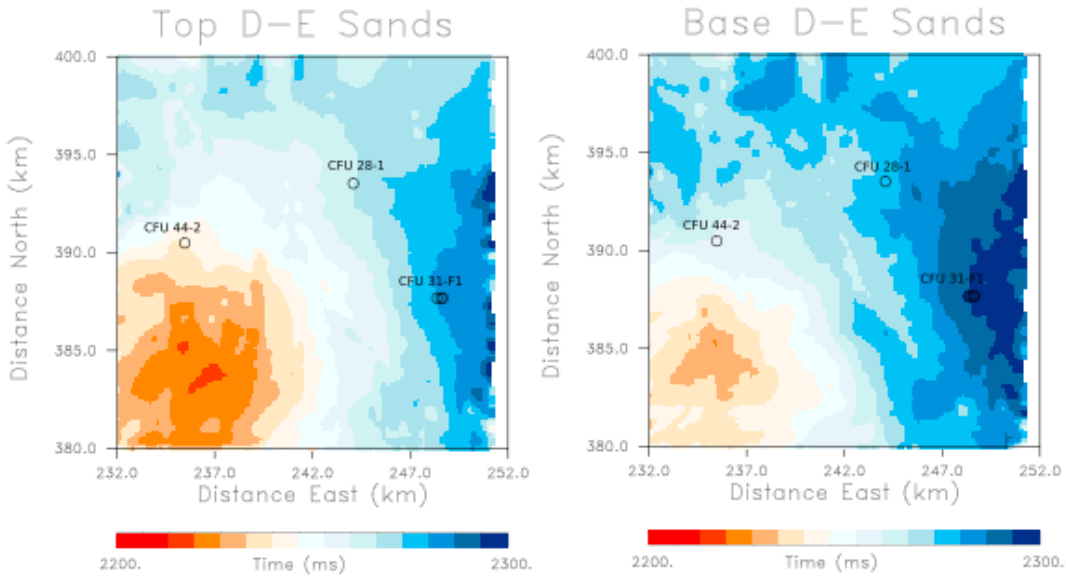

Figure 1. Picked horizons corresponding to the top and base of the reservoir at the Cranfield site. The open circles denote the locations of three wells where complete sonic logs were available.

2.5 Reservoir Modeling and Characterization

Reservoir simulation has been an important component of the Department of Energy's Cranfield project. For example, a recent full field simulation and characterization study utilized past production data, including average reservoir pressure and monthly oil and gas production rates and water cut, to develop an initial reservoir model (Alfi & Hosseini, 2016; Alfi et al., 2019). The approach is an extension of the more localized study of Hosseini et al. (2013). That work adopted a facies-based stochastic methodology in order to match the available historical production data. Four sandstone and four shale operational facies were derived, each with a constant porosity, permeability, and geobody shape [Hosseini et al. (2013). Commercial software was used to generate multiple, equally likely, geostatistical realizations featuring channels and barriers. Initially, the facies were conditioned to hard data at the wells and calibrated to match monthly oil and gas production rates, water cut, and average reservoir pressure for the early life of the field from 1944 until 1966 (Alfi & Hosseini, 2016). A second step involved matching oil, water, and gas production from June 2008 until August 2010 by changing parameters in the model that will not affect the initial history match. Thus, properties such as the minimum miscibility pressure, density, and viscosity of carbon dioxide in the reservoir were varied to fit the observations. The resulting model fit the EOR production data reasonably well. In addition, the model was able to produce an acceptable match to the CO_2 breakthrough times (Alfi & Hosseini, 2016).

3 Methodology

In this section we outline the techniques underlying our seismic data analysis. For the most part, the methods that we shall employ are conventional seismic data analysis with modifications for our application to the Cranfield site. Our time shift estimates follow from the correlated leakage method (CLM) of Whitcombe et al. (2010). They represent the changes in two-way travel time between baseline and monitor traces, for a time window located just below the reservoir interval. The time shifts are calculated after first aligning the traces using reflections from a time interval just above the reservoir. For our modeling of the seismic response to fluid injection and production, we extend conventional Biot theory to allow for an arbitrary number of fluid components. In the next section we provide additional details related to our application to the Cranfield field observations.

3.1 Estimating Seismic Amplitude Changes

At the Cranfield site the seismic data are provided as a pair of three-dimensional cubes with two spatial dimensions, the cross-line and in-line directions, and one time dimension representing two-way travel time. The baseline cube contains seismic traces from a survey prior to the injection of carbon dioxide while the monitor cube was obtained from seismic data gathered roughly 2 years after the start of injection. The injection, though it started in July 2008, was staged so that areas in the northeastern part of the field had experienced less than a year of injection by the time of the follow-on survey in 2010. The two data sets were processed independently, which limited the precision of the estimated time-lapse changes. Estimates of seismic amplitude changes follow from direct differencing of the baseline and monitoring traces of the seismic cubes. However, before this step, one must correct for differences that are unrelated to changes in the reservoir. Most seismic surveys rely on temporary arrays of receivers, rather than on permanent stations, and thus the exact geometry of the initial survey is not replicated, leading to differences that are not related to the injection of carbon dioxide. Differences in instrumentation are also possible, and seismic source repeatability is an issue. Furthermore, due to seasonal and climatic factors, the near surface conditions can also differ and produce differences between the baseline and monitor traces. In order to mitigate these effects, the baseline and monitor surveys are processed in such a manner that the differences due to nonreservoir factors are minimized. Such cross-equalization attempts to correct for differences in frequency content, amplitudes, and variable time shifts that are not related to reservoir processes.

The next step is to determine the seismic amplitudes that are associated with reflections from the reservoir itself. Such reflections are typically determined from wells logs and then picked from a continuous set of peaks or troughs defining the boundary. In the case of the Cranfield data we consider the reflection from the top of the reservoir. The amplitude change is assumed to be due to changes in the velocity of the reservoir induced by fluid injection and production. This assumption is supported by both

crosswell seismic imaging and by vertical seismic profile monitoring (Ajo-Franklin et al., 2013; Daley et al., 2014). For a thin reservoir, such as the D-E sandstone unit of the lower Tuscaloosa Formation at Cranfield, there may be interference between the top and bottom reflection of the reservoir (Zhang et al., 2014).

3.2 Travel Time Shifts

Velocity changes within the reservoir will also change the propagation time for seismic waves traveling through the reservoir, producing time shifts for reflections from interfaces beneath the reservoir (Zhang et al., 2013b). Such time shifts have been observed and utilized at other fields, such as Sleipner (Furre et al., 2015) and Weyburn (White et al., 2011; White, 2013a). Note that the factors cited above, changes in sensor location, near surface velocity variations, and geomechanical effects can also lead to time shifts throughout the seismic section. Several of these factors are dealt with at the cross-equalization stage, where global and distinct trace time shifts may be introduced to account for near surface and geomechanical processes. As an additional step, we align a segment of the traces, for a window that extends from just above the reservoir to several reflectors above this boundary. We estimate and apply the time shift necessary to align the traces for this segment. We then apply that shift to the portion of the trace that is below the reservoir. The resulting time shift between the two traces for the window below the reservoir is assumed to be due to velocity changes within the reservoir at the location of the trace. Recall that the processing involved in stacking the seismic traces and generating the seismic cubes will introduce errors and artifacts in the travel time shifts, so the estimate is approximate (Kanu et al., 2016).

The CLM provides estimates of travel time shifts (Whitcombe et al., 2010) for the time intervals above and below the reservoir. The technique was motivated by the observation that many images of seismic time-lapse changes appear to contain a coherent pattern that leaks into the difference. The leakage can be attributed to two main sources, amplitude scaling differences and small time shifts that may vary over the image. The correlation leakage method seeks to estimate the time shifts by plotting the difference between the baseline and the monitor survey, against the difference between the average of the two surveys and a time shifted version of this average. The slope of a line fit to this plot provides an estimate of the time shift between the baseline and monitor surveys. The technique yields accurate estimates if the time shift between the traces is small, and there are no large amplitude variations or waveform changes between the two seismic surveys. One can normalize the traces within the window of interest in order to account for amplitude variations.

Though the description given above may sound complicated, the derivation is relatively simple. We present a slight modification of the derivation provided by Whitcombe et al. (2010). The primary assumption is that, within

a time window of interest, a trace from the monitor survey $M(t)$ is a time shifted version of the trace from the baseline survey $B(t)$. Thus, if the baseline trace is $B(t)=S(t)$, then the monitor survey is $M(t)=S(t+\tau)$, where τ is the shift within the time window. If we consider the difference between the respective baseline and monitor surveys for an identical location, and within the time window of interest, then

$$M(t) - B(t) = S(t+\tau) - S(t), \quad (1)$$

Using a Taylor series expansion to approximate $S(t+\tau)$ gives

$$M(t) - B(t) \approx \tau \left[\dot{S}(t) + \frac{1}{2}\tau\ddot{S}\right], \quad (2)$$

where the dots signify derivatives with respect to time. Now consider the average of the baseline and monitor surveys

$$\sigma(t) = \frac{1}{2}\left[M(t) + B(t)\right] = \frac{1}{2}\left[S(t+\tau) + S(t)\right], \quad (3)$$

and the average of these traces shifted by a time increment δt

$$\sigma(t+\delta t) = \frac{1}{2}\left[S(t+\delta t+\tau) + S(t+\delta t)\right]. \quad (4)$$

Expanding both terms on the right-hand side of equation 4 in a Taylor series, to first order in δt, gives

$$\sigma(t+\delta t) \approx \frac{1}{2}\left[S(t+\tau) + \delta t\dot{S}(t+\tau) + S(t) + \delta t\dot{S}(t)\right]. \quad (5)$$

Subtracting the average in equation 3 from that of equation 5 produces the reduced expression

$$\sigma(t+\delta t) - \sigma(t) \approx \frac{\delta t}{2}\left[\dot{S}(t+\tau) + \dot{S}(t)\right]. \quad (6)$$

A Taylor series expansion of the term $\dot{S}(t+\tau)$ in equation 6 results in the representation of this difference as

$$\sigma(t+\delta t) - \sigma(t) \approx \delta t\left[\dot{S}(t) + \frac{1}{2}\tau\ddot{S}(t)\right]. \quad (7)$$

Thus, if we form the ratio $[\sigma(t+\delta t) - \sigma(t)] / [M(t) - B(t)]$, the quantities in square bracket in equations 2 and 7 cancel and we are left with

$$\frac{\sigma(t+\delta t) - \sigma(t)}{M(t) - B(t)} = \frac{1}{\tau}\delta t. \quad (8)$$

Equation 8 describes a linear function in terms of the shift increment δt with the slope given by the inverse of the time shift τ between the two traces. Thus, we can fit a line to a set of points with components $\sigma(t+\delta t)-\sigma(t)$ and $M(t)-B(t)$ as a function of δt and use the slope of this line to determine τ (Whitcombe et al., 2010). This technique has been applied to both synthetic and field data and compared to several other methods, including standard cross-correlation, a nonlinear inversion method (Rickett et al., 2007),

dynamic warping (Hale, 2013), and multiscale and iterative refinement optical flow (Zhang & Du, 2016) for both prestack zero-offset time-lapse traces and poststack migrated time-lapse traces (Kanu et al., 2016). The CLM approach was found to work better then standard cross-correlation and nonlinear inversion (Kanu et al., 2016; Whitcombe et al., 2010; Zhang et al., 2013b)

3.3 Rock Physics Estimates

The saturation changes within the reservoir due to production and injection typically introduce changes in its elastic properties. For example, the injection of carbon dioxide into a brine saturated porous medium will lower the velocity of compressional waves that propagate across it. Such velocity variations also lead to changes in the reflective character of the reservoir over time. These time-lapse variations may be used to monitor saturation changes, a common practice in oil and gas fields (Calvert, 2005). Fortunately, there are long-standing theoretical approaches for estimating the changes in the elastic properties of a porous rock subject to changes in fluid content, based upon the work of Gassmann (1951) and Biot, (1956a, 1956b). The approach gives acceptable results at the seismic frequencies that we will consider, roughly around 30 Hz.

There are other factors besides fluid saturation changes that can influence seismic properties within and around a producing reservoir. For example, geomechanical effects have been noted at the Cranfield site (Kim & Hosseini, 2013), but the observed seismic velocity changes associated with fluid pressure variations are small (Marchesini et al., 2017). Geochemical effects are also possible and can influence the moduli of reactive formations, but we will not consider such processes at this time because they are thought to play a minor role at Cranfield (Lu et al., 2012b). Finally, we do not consider the amplitude changes that injected supercritical carbon dioxide can generate by increasing the seismic intrinsic attenuation.

3.3.1 Gassmann's Equations

The original formulation of Gassmann's theory, for a rock consisting of mono-mineralic spherical grains, provides a formula relating the bulk modulus of the unsaturated material, K_u, to the bulk modulus of the rock saturated with a fluid with bulk modulus K_{fluid}

$$K_{sat} = K_u + \frac{\left(1 - K_u/K_{grain}\right)^2}{\varphi/K_{fluid} + (1-\varphi)/K_{grain} - K_u/K_{grain}^2}, \quad (9)$$

where φ is the porosity and K_{grain} is the bulk modulus of the grains (Smith et al., 2003). According to Gassmann's approach, the shear modulus of the saturated rock, G_{sat}, is not influenced by the presence of the pore fluid and thus $G_{sat}=G_u$, where G_u is the shear modulus of the unsaturated rock. The density of the rock is a simple weighted average of the solid and fluid densities

$$\rho_{sat} = (1-\varphi)\,\rho_{grain} + \varphi\rho_{fluid}, \quad (10)$$

The compressional velocity for the saturated rock is given by standard expression (Aki & Richards, 1980)

$$V_p^{sat} = \sqrt{\frac{K_{sat} + \frac{4}{3}G_{sat}}{\rho_{sat}}}, \quad (11)$$

The seismic velocity changes will influence the propagation time of elastic waves traveling through the reservoir. In addition, the saturations changes will alter the reflection coefficient of the layer by modifying its acoustic impedance

$$I_{sat} = \rho_{sat} V_p^{sat}. \quad (12)$$

Gassmann's approach was originally developed for a single saturating fluid, and so the bulk modulus K_{fluid} and density ρ_{fluid} are simply identified with those of the fluid. If we wish to extend the approach to fluid mixtures, then we must adopt a strategy for averaging the bulk moduli of the fluid constituents. This is a subject of considerable depth (Mavko et al., 1998), and we can only mention a few important points that relate to our analysis of the Cranfield data. The density of the composite fluid, ρ_{fluid}, is given by the saturation-weighted sum of the component densities

$$\rho_{fluid} = S_g\rho_g + S_o\rho_o + S_w\rho_w, \quad (13)$$

where *g*, *o*, and *w* signify the gas, oil, and water phases, respectively. The bulk modulus for the composite fluid is more complicated because it depends upon the distribution of the fluids at scales that are less than a seismic wavelength. Intuitively, one can understand how the strength of a composite material can depend upon how the constituents are arranged with respect to the direction of compression or extension. For example, assuming no flow between the fluids, if the components are a stack of layers perpendicular to the direction of propagation, then the strength of the composite is controlled by the weakest material and the effective modulus is given by

$$K_{fluid} = K_{Reuss} = \left[\sum \frac{S_i}{K_i}\right]^{-1}, \quad (14)$$

the Reuss average of the fluid moduli. This average is also appropriate for fluids that are well mixed within a representative elementary volume, such as a core. The Reuss average provides a lower bound on the composite fluid modulus. Alternatively, if the component fluids are distributed in layers aligned with the direction of propagation, then the effective modulus is controlled by the strongest material. The modulus for such a composite material is the weighted sum

$$K_{fluid} = K_{Voigt} = \sum S_i K_i, \quad (15)$$

an upper limit on the effective bulk modulus known as the Voigt bound. Similar considerations also apply to other directional processes such as heat flow in a composite material (Wiener, 1910). In addition to these upper and lower bounds, the Hill estimate given by the average of the two extreme models,

$$K_{Hill} = \frac{1}{2}\left[K_{Reuss} + K_{Voigt}\right], \quad (16)$$

is often used as a representative model (Mavko et al., 1998). The variations in compressional velocity that result from the use of these three composite moduli are shown in Figure 2 for parameters that are appropriate for the Cranfield area. Note that the variation between models is almost as large as the total change in compressional velocity due to the introduction of carbon dioxide.

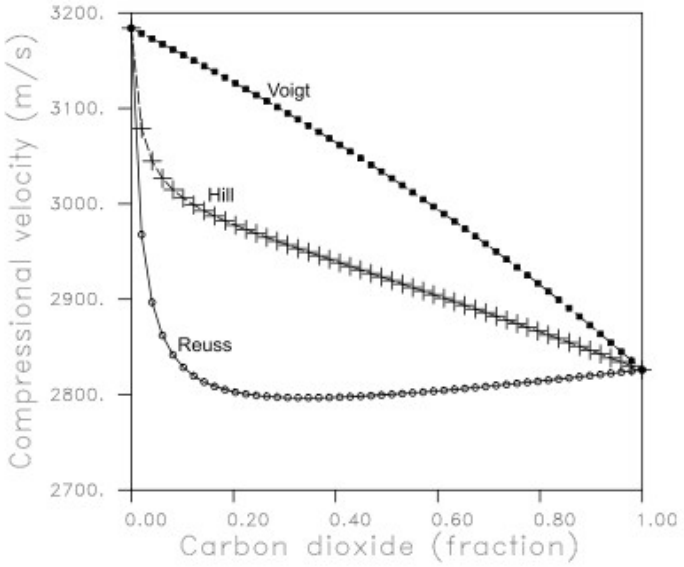

Figure 2. Modeled variation in compressional wave velocity as a function of the saturation of carbon dioxide within the pore space. The results correspond to the case in which there is only water in the initial porous medium. The three curves correspond to different techniques for averaging the fluid moduli for the water and the carbon dioxide (see equations (14) and (15)).

For a sedimentary geologic environment one would expect that fine-scale layering would provide the most common setting for distributing fluids in a heterogeneous fashion, perhaps augmented by density and gravitational effects. Thus, for horizontal layers and vertically propagating waves the Reuss average 14 would appear to be the most appropriate. However, a poststack seismic cube is a combination of waves propagating in a variety of directions with respect to the layering. Furthermore, there are factors such as dipping layers, oriented fracture sets, and other forms of heterogeneity that will further complicate the situation. The important point is that it can be difficult to determine how to average the fluid moduli in order to estimate K_{fluid} accurately.

3.3.2 An Extension of Biot Theory

The next level of sophistication incorporates the dynamics of fluid movement into estimates of the composite modulus and seismic velocities. Thus, the seismic velocities will depend upon the flow properties of the medium, such as permeability, and the properties of the fluids. The case of a single fluid in an elastic porous medium was treated in the pioneering work of Biot, (1956a, 1956b). This work has been extended to two well mixed fluids by Berryman et al. (1988). A recent derivation that allows for smoothly varying properties and three fluid phases (Vasco, 2013) was formulated in a manner that is easily extended to a medium containing additional fluids. Thus, as demonstrated in the appendix, one can generalize the formulation to allow for N_f fluid phases, making it applicable to the situation at Cranfield where we have brine, oil, methane, and carbon dioxide as the primary fluids. The poroelastic medium is characterized by the porosity φ, and the fraction of solid per unit volume is

$$\alpha_s = 1 - \varphi \quad (17)$$

while the fraction of the volume occupied by the nth fluid is

$$\alpha_n = \varphi S_n, \quad (18)$$

In the case of N_f fluid phases one can produce N_f+1 equations governing the solid and fluid displacements in the frequency domain $\mathrm{U}(x,\omega)$ and $\mathrm{W}_n(x,\omega)$, $n=1,2,\ldots,N_f$. Note that the first expression actually represents N_f equations as we cycle through n from 1 to N_f,

$$\begin{aligned} \nu_n \mathbf{U} + \Gamma_n \mathbf{W}_n &= \nabla \left[C_{ns} \nabla \cdot \mathbf{U} + \sum_{j=1}^{N_f} M_{nj} \nabla \cdot \mathbf{W}_n \right], \\ \nu_s \mathbf{U} + \sum_{j=1}^{N_f} \xi_j \mathbf{W}_j &= \nabla \left[K_u \nabla \cdot \mathbf{U} + \sum_{j=1}^{N_f} C_{sj} \nabla \cdot \mathbf{W}_j \right] + \nabla \cdot \boldsymbol{\tau}. \end{aligned} \quad (19)$$

The deviatoric stress tensor, τ, is given by linear elasticity (Wang, 2000)

$$\boldsymbol{\tau} = G \left[\nabla \mathbf{U} + \nabla (\mathbf{U})^T - \frac{2}{3} \nabla \cdot \mathbf{U} \mathbf{I} \right] \quad (20)$$

for a solid matrix with shear modulus G. The poroelastic parameters are analogous to those found in the study of a single fluid phase in a poroelastic medium (Pride, 2005; Wang, 2000): K_u (undrained bulk modulus), C_{ns} and C_{sj} (Biot coupling moduli), and M_{nj} (fluid storage coefficients). Their relationship to the properties of the medium, specifically the relative permeability functions, the capillary pressure curves, the fluid, and rock properties, are given in Vasco (2013) for three fluid phases and are easily generalized to the case of N_f fluids. The other constants are related to the frequency, the solid and fluid fractions, and the solid and fluid properties,

$$\nu_s = \alpha_s \rho_s \omega^2, \quad (21)$$

$$\nu_n = \alpha_n \rho_n \omega^2, \quad (22)$$

$$\xi_j = \alpha_j \rho_j \frac{\mu_j}{k_j(\omega)} \omega, \quad (23)$$

$$\Gamma_n = \alpha_n \rho_n \left[\omega - \frac{\mu_n}{k_n(\omega)} \right] \omega, \quad (24)$$

ρ_s is the solid density, ρ_n is the density of the nth fluid, μ_n is the viscosity of the nth fluid, and $k_n(\omega)$ is the dynamic permeability discussed in the appendix (see equation A10). As shown in the appendix, for a reservoir with lateral deviations in properties that vary smoothly in comparison to the seismic wavelengths, it is possible to construct an explicit expression for the squared slowness $s=p^2$ associated with the propagation of longitudinal modes. Specifically, s satisfies the polynomial equation that results from the vanishing of the determinant

$$\det \begin{bmatrix} \nu_s - Hs & \xi_1 - C_{s1}s & \cdots & \xi_{N_f} - C_{sN_f}s \\ \nu_1 - C_{1s}s & \Gamma_1 - M_{11}s & \cdots & -M_{1N_f}s \\ \vdots & \vdots & \ddots & \vdots \\ \nu_{N_f} - C_{N_f s}s & -M_{N_f 1}s & \cdots & \Gamma_{N_f} - M_{N_f N_f}s \end{bmatrix} = 0, \quad (25)$$

where $H=K_u+4/3G$. The roots of the polynomial determine the squared slownesses and the phase velocities of the fast and slow compressional waves in the poroelastic medium follow from the expression

$$C = \frac{\omega}{p}, \quad (26)$$

The poroelastic properties of the reservoir, the properties of the fluids, the frequency, and the fluid saturations are necessary in order to calculate all of the parameters in equation 25. As noted in Vasco (2013), there are 12 fundamental classes of parameters that are needed in order to define the coefficients.

As in the work of Gassmann (1951), complications ensue due to inhomogeneous distributions of two or more fluids, as in the patchy saturation of White (1975) and others (Dutta & Ode, 1979; Johnson, 2001; Norris, 1993). A comprehensive treatment was provided by Pride et al. (2004) in terms of mesoscopic spatial variations in properties, that is, variations at length scales between the microscopic grain scale and the macroscopic length scale of the seismic waves. Such heterogeneity can account for the actual level of seismic attenuation observed within porous sediments (Pride, 2005). The patchy saturation approach has been applied to crosswell seismic data at Cranfield (Ajo-Franklin et al., 2013). As indicated in Figure 10 of Ajo-Franklin et al. (2013), the surface seismic data examined in this study are in the low-frequency limit for patches of reasonable sizes. This results in variations that corresponds to the Reuss curves shown here and the phase velocity given by equations 25 and 26,

4 Data Analysis and Results

In this section we present an analysis of the Cranfield time-lapse seismic amplitude changes and travel time shifts. We use the rock physics techniques described earlier, in tandum with reservoir simulation results, to calculate expected changes in amplitudes and time shifts, and compare those changes with observed values. We begin with a discussion of available wells logs and the construction of a model of elastic properties for the overburden.

4.1 Well Logs and Seismic Velocity Variations

Spontaneous potential logs were run for all of the original 93 wells in the field and used for correlation and mapping the net sandstone in the field (Kordi, 2013). Other selected wells have more comprehensive suites of logs, including shallow and deep resistivity and gamma ray observations. However, the set of wells containing sonic logs measuring seismic velocities, particularly in the overburden, is rather limited. In fact, the only reliable sonic log data were from the three widely distributed wells indicated in Figure 1. Two additional sonic logs were gathered at Wells CFU 31-F2 and CFU 31-F3, shown as unmarked circles adjacent to well CFU 31-F1 in Figure 1, but issues with the drilled holes and casing-deployed instrumentation made their interpretation difficult (Butsch et al., 2013). In order to determine those features of the vertical velocity variation that are robust, we did a pairwise correlation between the well logs, as shown in Figure 3. The nonlinear inversion method of Rickett et al. (2007) was used to find the depth-varying shift that produces an optimal correlation between the well logs. In this approach one finds the depth shift function that minimizes the misfit between two traces, subject to a spatial penalty term that enforces a smoothness requirement on the solution. The three compressional sonic logs, with the optimal depth shifts are plotted together in Figure 4. In general, the large-scale depth variations are shared by the well logs, even though the wells are many kilometers apart. The average of the three shifted traces is also shown in Figure 4. Though there can be biases when comparing surface seismic velocities to sonic logs (De et al., 1994), there is rough agreement between the average of the well logs and the average velocities used to form the seismic cubes, also plotted in Figure 4. In particular, there is no significant offset between the two velocity trends, as can sometimes occur due to the very different sources of velocity information. This average velocity variation in the overburden will be used to generate synthetic seismograms and to calculate the reflection amplitude changes and time shifts due to the injection and production activities.

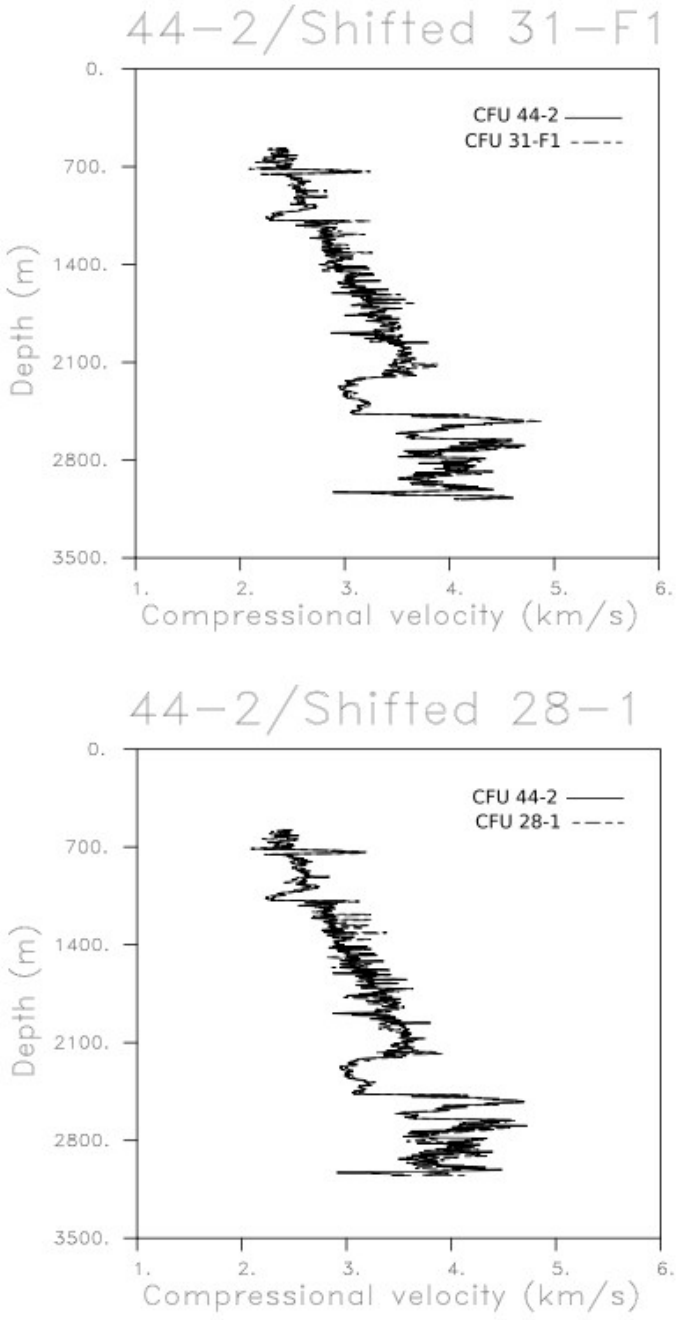

Figure 3. (Upper panel) Compressional wave sonic logs from wells CFU-44-2 and CFU 31-F1. Depth-varying length changes have been applied to the well log from CFU 31-F1 in order to optimize its correlation with well CFU-44-2. The length changes were estimated using the nonlinear inversion method of Rickett et al. (2007). (Lower panel) Well logs from CFU-44-2 and CFU 28-1, where the log from CFU 28-1 has been stretched and compressed in depth to optimize their similarity.

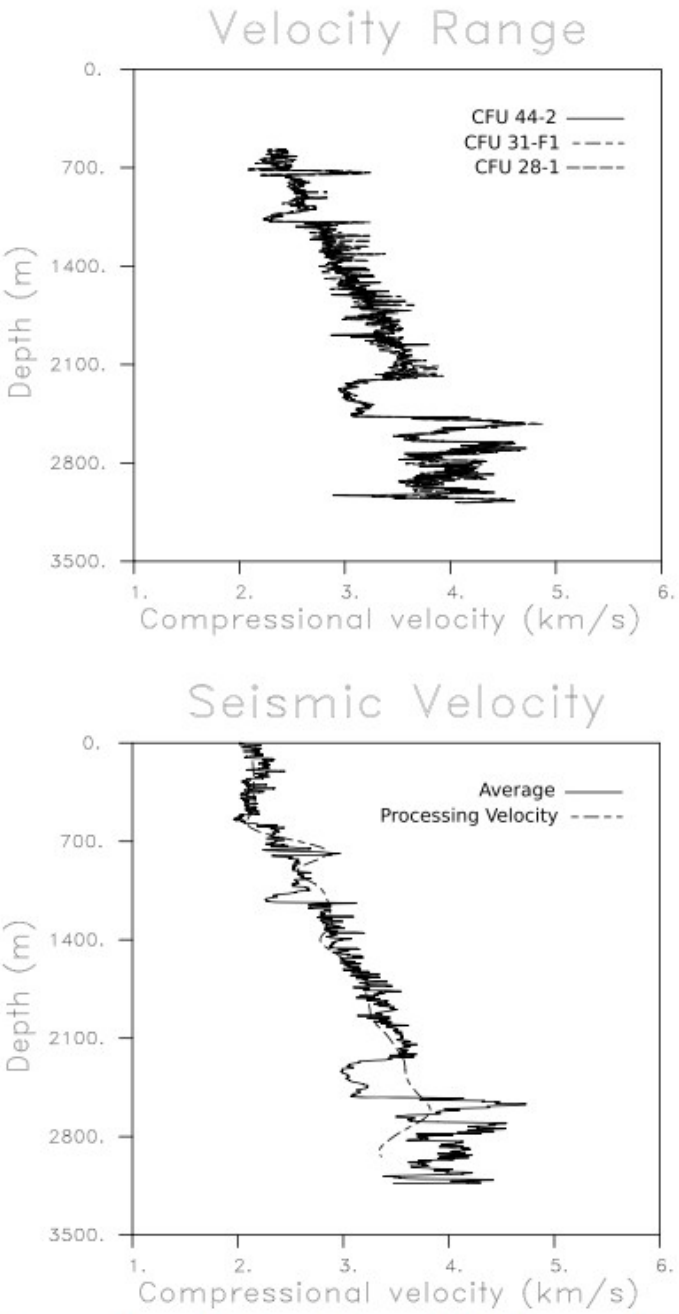

Figure 4. (Upper panel) Compressional sonic logs from the three wells plotted in Figure 1. The sonic logs from wells CFU 31-F1 and CFU 28-1 have been subject to depth-varying shifts in order to maximize agreement with the variations observed in well CFU 44-2. (Lower panel) The average of the three sonic logs shown above (solid line) plotted along with an average of the compressional velocities used in the analysis of the surface seismic data.

4.2 Time-Lapse Changes

4.2.1 Amplitudes

The time-lapse cubes provided by GeoTrace have been processed to correct for static errors that could cause differences between the two surveys and to account for variations in the spectral content of the traces that result from

inconsistencies in the sources and near surface velocities (Ditkof, 2013; Zhang et al., 2013a). Our interest lies in the changes in reflections from the reservoir boundaries and how these might be related to changes in reservoir fluid content. In Figure 5 we plot amplitudes corresponding to the reflections from the top boundary of the reservoir. The large negative values are indicative of the velocity decreases associated with the D-E sandstone unit of the lower Tuscaloosa Formation comprising the reservoir. The large-scale pattern of amplitudes is similar for both the baseline (2007) and monitor (2010) surveys. However, there are some obvious differences in amplitude between the two surveys. For example, a swath of positive amplitude values to the north and east of well CFU 44-2 in the 2007 survey turns to mostly negative amplitudes in 2010.

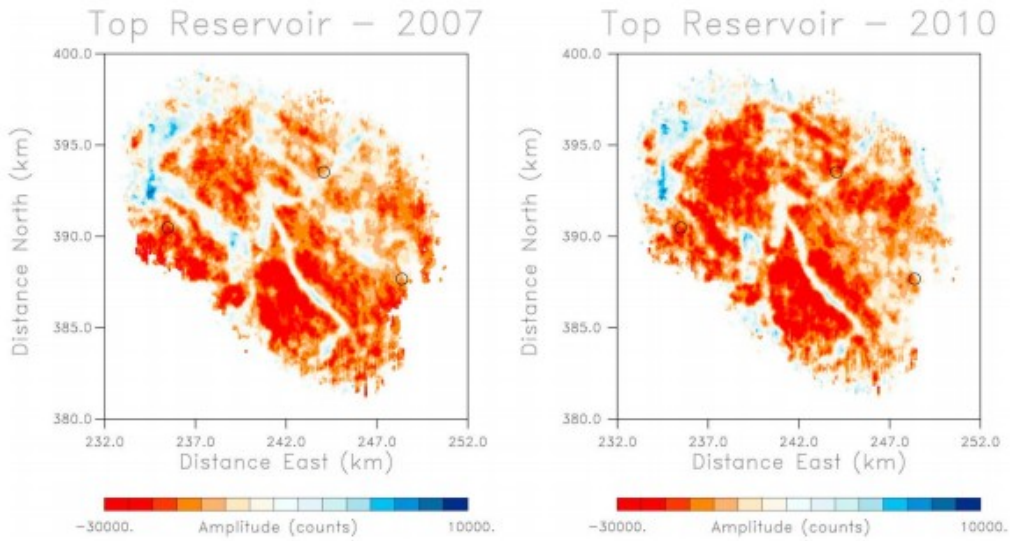

Figure 5. (Left panel) Reflection amplitudes from the top of the reservoir for the 2007 baseline survey. The open circles denote the three wells plotted in Figure 1. (Right panel) Corresponding seismic amplitudes from the 2010 monitor survey.

The time-lapse changes, shown in Figure 6, are obtained by subtracting the preinjection baseline trace values from the monitor survey values. There is considerable spatial variation in the seismic amplitude changes, though there is a systematic negative amplitude change where there is good repeatability, away from the edges of the survey volume (Ditkof et al., 2013; Zhang et al., 2013a). Because the injected carbon dioxide lowers the seismic velocity, we would expect that the monitor survey would be larger in magnitude but negative in sign, leading to a large negative time-lapse difference. The locations of wells in the northeast quadrant of the reservoir that injected carbon dioxide during the 3-year interval between 2007 and 2010 are plotted in Figure 6 as open circles. There is some correspondence between the location of the injected carbon dioxide and the time-lapse changes, but there are also changes some distance away from the injection wells. We will interpret the changes in the northeast section of the field in greater detail below. Again there are notable spatial variations in the

reflection amplitudes, suggesting significant heterogeneity in reservoir properties and fluid saturations.

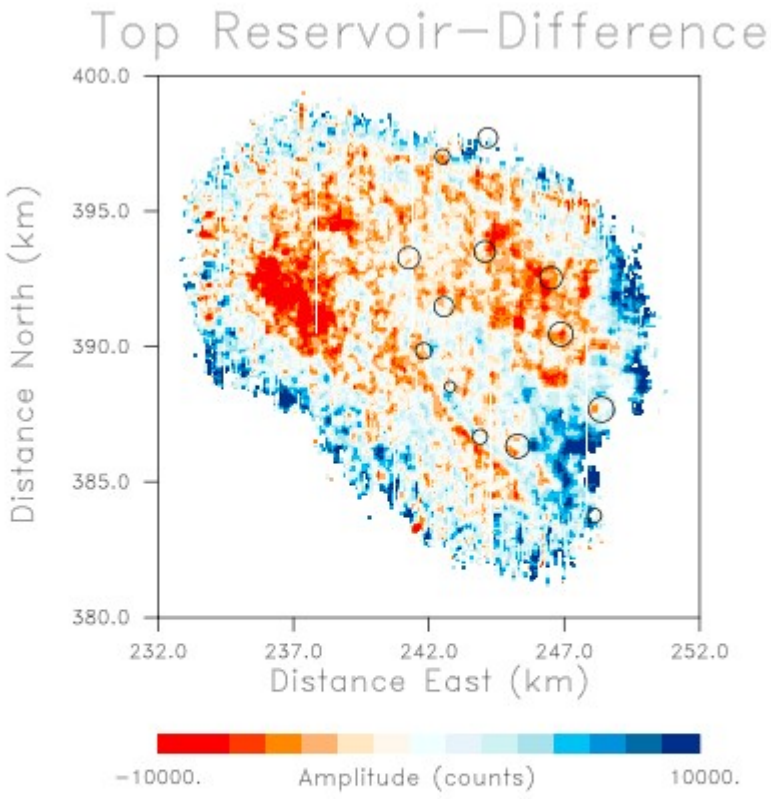

Figure 6. The differences in seismic amplitudes formed by subtracting the values of the baseline survey from those of the monitor survey. The open circles denote the three wells plotted in Figure 1 and the main carbon dioxide injection wells operating in the northeast corner of the field between 2008 and 2010. The diameter of the circles is proportional to the volume of injected carbon dioxide.

4.2.2 Time Shifts

The velocity changes due to the injected carbon dioxide will lead to time shifts for waves propagating through the reservoir. Using the CLM, described in the methodology section, we quantify and image these time shifts. In order to isolate the time shifts due to velocity changes within the reservoir from those that are due to changes within the overburden and near surface variations, we first line up the baseline and monitor traces for a time window just above the reservoir. The idea can be illustrated using the traces in Figure 7. Based upon the surfaces in Figure 1, defining the top and bottom of the reservoir, we designate a 0.2-s time window, extending from 2.05 to 2.25 s. The window length was chosen to contain a sufficient number of reflections for an accurate measurement of the time shift, yet not extend too far from the reservoir boundaries. We use those portions of the baseline and monitor traces within this window to define the initial overburden time shift using the CLM approach.

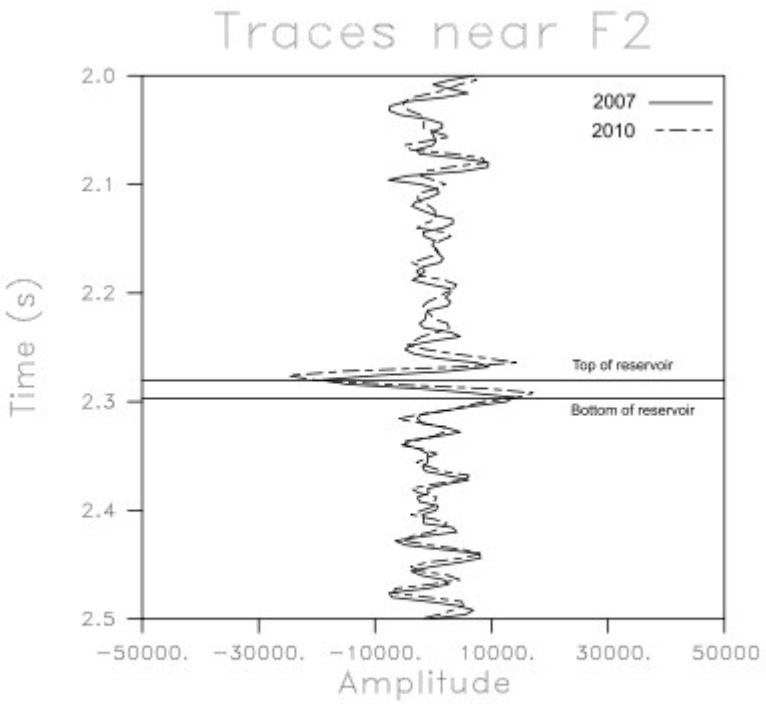

Figure 7. Traces from the baseline (2007) and monitor (2010) seismic data sets associated with a location near well CFU 32-F2. The top and bottom of the reservoir are denoted by the horizontal lines.

Next, the entire trace is corrected by the overburden shift, and a second window is defined, comprising reflections from layers just below the reservoir. We are interested in the time shift between the two traces that occurs within this window, as it should be more closely tied to velocity changes within the reservoir itself. The CLM is used to calculate the time shift within the 0.2-s time window. We have adopted a sign convention such that a positive time shift is associated with a delay in the monitor trace, as would be induced by a lowering of the velocity within the reservoir interval. With this convention a positive time shift corresponds to a pull-down of the layers below the reservoir. The time shifts for the entire area covered by the two seismic surveys are shown in Figure 8. As with the amplitude changes, there is considerable spatial variation and significant changes at large distances from the wells. Generally, there are notable time shifts beneath the injection wells that we have plotted in the northeastern part of the field.

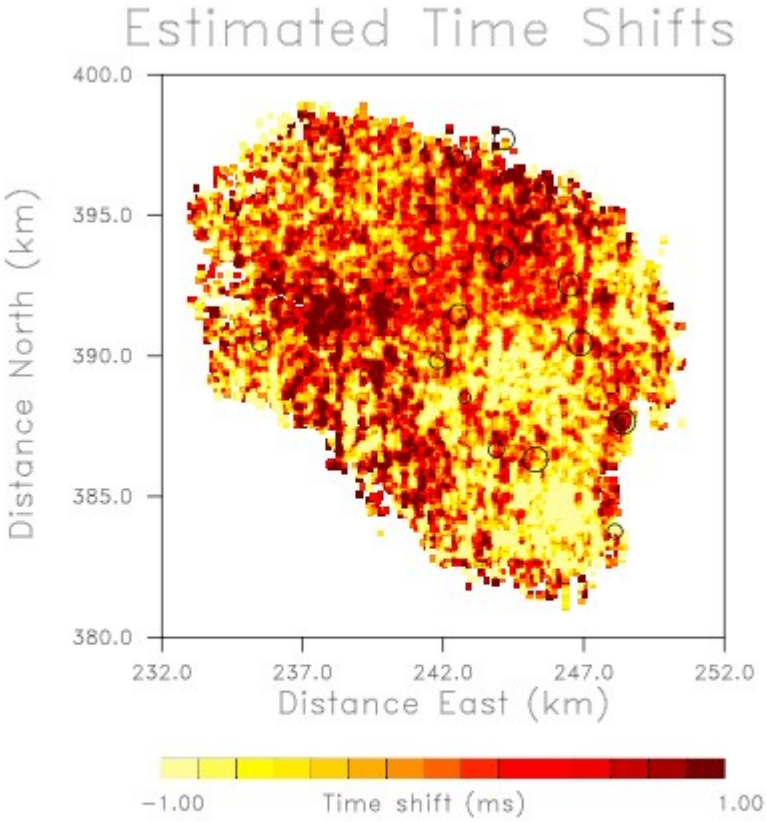

Figure 8. Time shifts associated with reflections from interfaces just below the reservoir. The time shifts were calculated using the correlated leakage method of Whitcombe et al. (2010). The open circles denote the three wells plotted in Figure 1 and the main carbon dioxide injection wells operating in the northeast corner of the field between 2008 and 2010.

4.3 Multicomponent Reservoir Modeling

There are many factors controlling the seismic velocity changes due to the injection of a volume of carbon dioxide. Without some guidance from reservoir modeling, it can be difficult to understand the complicated patterns of amplitude changes and time shifts observed in Figures 6 and 8, respectively. Fortunately, a significant part of the monitoring program at Cranfield involved reservoir modeling (Alfi & Hosseini, 2016; Delshad et al., 2013; Hosseini et al., 2013), and this work can aid in our interpretation of the seismic observations. Recently, we used the computer modeling group's compositional simulator CMG-GEM to develop an improved reservoir model of the northeastern corner of the field. The model consists of seven different chemical components, including carbon dioxide, and incorporates fine-tuned properties that were appropriate for the Cranfield site, as published by Weaver and Anderson (1966). A cartesian grid, containing 82,559 cells, provides a numerical representation of the reservoir. The grid extends from a sealing fault, at its western edge, to deep within the aquifer at the northern and eastern boundaries. Vertically, the reservoir is partitioned into 12 layers,

with each layer 1.2 m thick. The starting porosity and permeability models were those of Hosseini et al. (2013), and these values were adjusted to match over 4 years of reservoir data, from July 2008 to October 2012. The observations, monthly oil, brine, and gas production data and CO_2 breakthrough times were fit by modifying the relative permeability data and by adjusting the location and flow properties of high-permeability channels within the model.

The best fitting reservoir model was then used to simulate the evolution of oil, brine, and total gas at the Cranfield site, from the start of production in 2008 until the follow-on seismic monitor survey in 2010. The average fluid pressure distributions within the reservoir in 2008 and 2010 are shown in Figure 9. Three phases are present at the start of injection: brine, oil, and a gas composed primarily of methane. Since the methane can dissolve into the oil, it is also distributed within the oil phase as a chemical component. In Figure 10 we plot the distribution of these three phases and the fraction of methane in the oil phase at the time of the baseline survey, averaged over the depth interval of the reservoir. At this point in the reservoir's history it has reached pressure equilibrium, some four decades after primary production. Methane gas has migrated updip and abuts the sealing fault to the west. Similarly, the remnants of the oil ring form a coherent accumulation bounded to the west by the sealing fault and the gas accumulation and bounded to the east by the aquifer. Saline pore water is distributed throughout the reservoir, but the highest saturation naturally occurs within the aquifer.

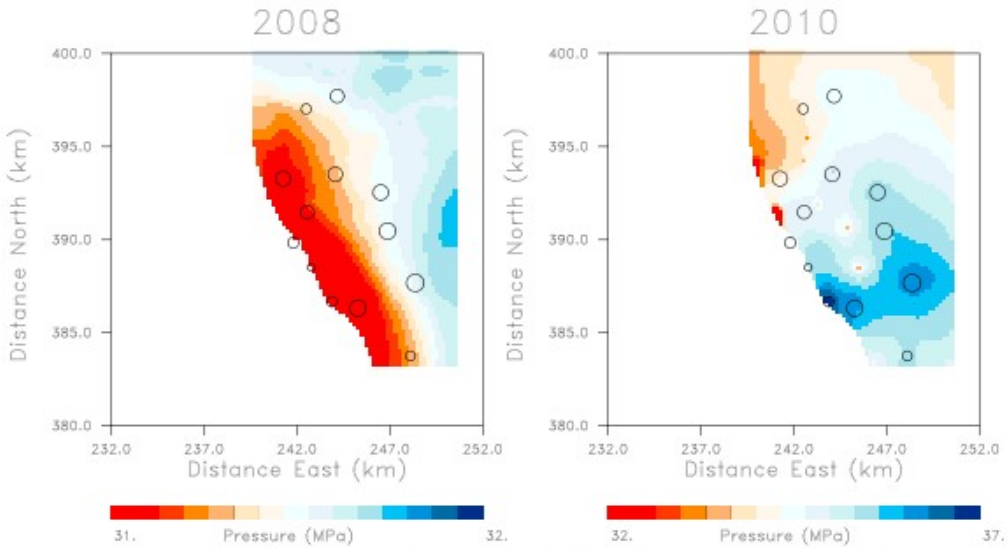

Figure 9. Maps of average fluid pressure for the beginning and end of the reservoir simulation. The open circles denote wells that injected carbon dioxide into the reservoir between 2008 and 2010.

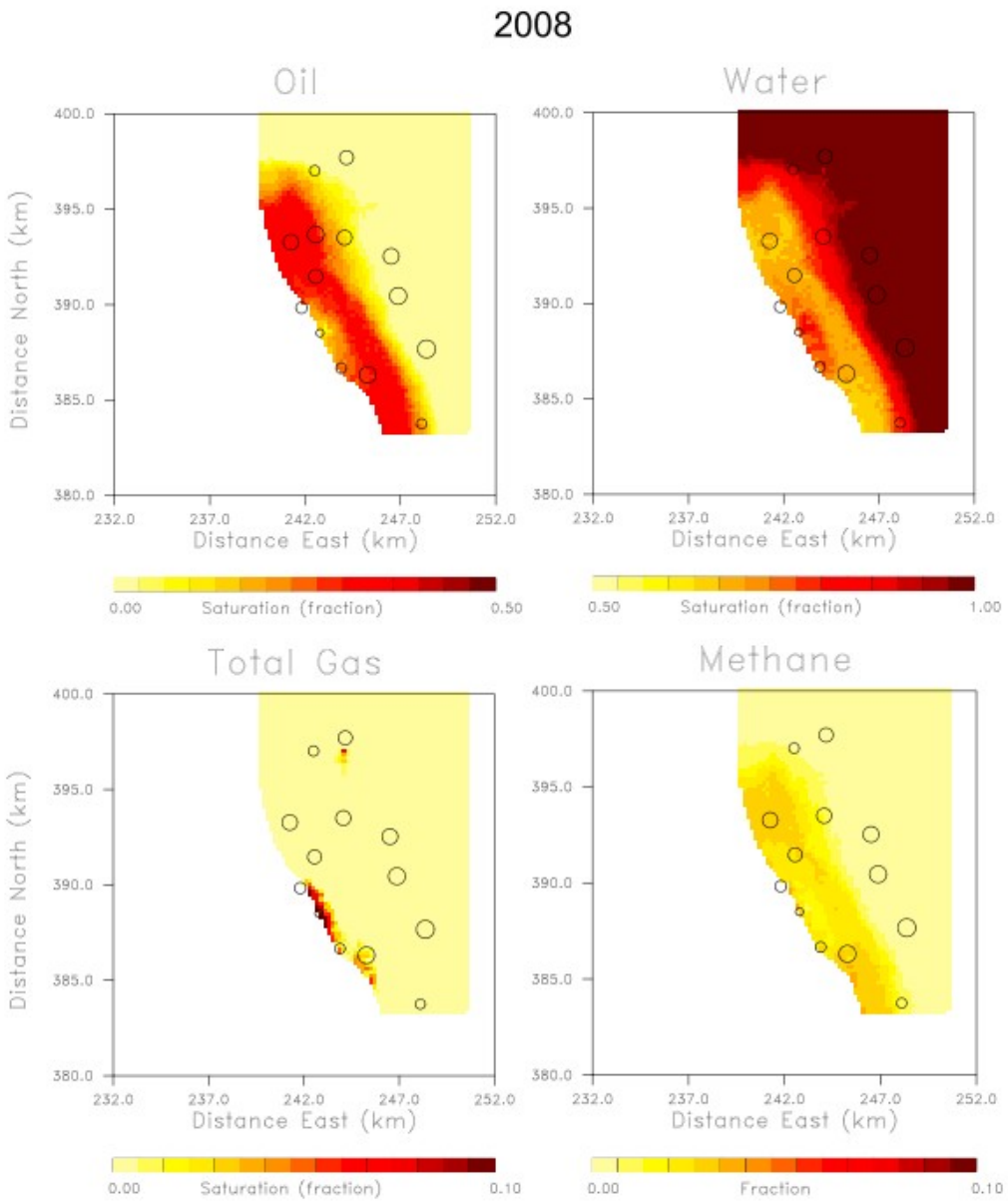

Figure 10. Maps of fluid saturations for oil, water, and total methane (gas) from a recent multicomponent reservoir simulation. The saturations are associated with reservoir conditions before the injection of carbon dioxide for enhanced oil recovery. The panel labeled methane denotes the fraction of dissolved methane in the oil. The open circles denote wells that injected carbon dioxide into the reservoir between 2008 and 2010.

After 3 years of oil and gas production, and the injection of over two million tons of carbon dioxide, the calculated fluid saturations have changed significantly (Figure 11). The total gas now consists largely of carbon dioxide, which is in a supercritical state and is distributed throughout the reservoir, both around the injection wells and at some distance from any injectors. Methane may also be present in a gaseous phase and often forms a bank ahead of the CO_2 fronts. The distribution of oil is broadly the same as it was in 2008, but there are pockets where there have been notable saturation

changes. The brine saturation is lower in much of the oil ring and generally in areas around the injectors, including within the aquifer. The methane fraction within the oil is more heterogeneous, as it has been redistributed by the injection and production in the area.

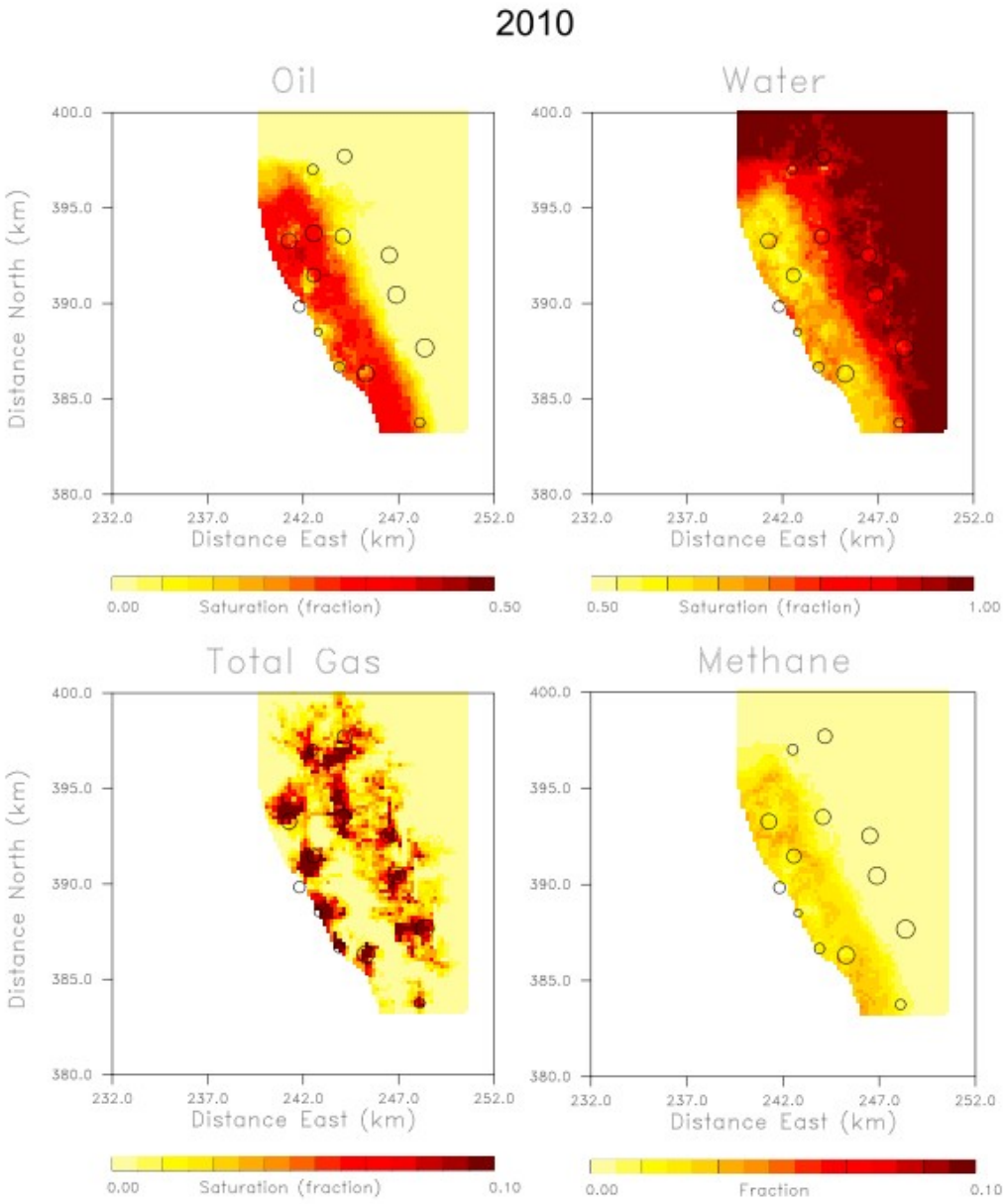

Figure 11. Oil, water, and total carbon dioxide (gas) saturations associated with reservoir conditions after 3 years of CO_2 injection and reservoir production, from 2008 to 2010. The panel labeled methane denotes the fraction of dissolved methane in the oil. The open circles denote wells that actively injected carbon dioxide into the reservoir during this time.

It should be noted that while the overall outlines of the fluid saturation distribution are robust, the detailed features are not well resolved. That is, the stochastic realization of the reservoir model is only constrained by widely spaced well data, field-wide production data, and carbon dioxide

breakthrough times. None of these observations provide fine-scale spatial resolution of the reservoir flow properties. Still, as we shall see in the next section, the larger-scale features do provide some insight into the factors that control the time-lapse seismic response.

4.4 Rock Physics Estimates of Time-Lapse Changes

Given the depth-averaged saturation distributions from the reservoir simulation, we can use the rock physics techniques from section 3 to estimate time-lapse seismic amplitude changes and time shifts. In order to do this, we need to specify the appropriate parameters in equations 9 and 10, as well as those in equation 25. As a simplifying assumption we ignore poroelastic effects outside of the reservoir where we have no information regarding fluid saturations. We use the average compressional velocities and densities from the shifted sonic and density logs from wells CFU 44-2, CFU 31-F1, and CFU 28-1 as an elastic model for the overburden. Only well CFU 44-2 had an accessible shear wave sonic log that covered the overburden, so it was necessary to use the shifts associated with the compressional velocity log to align it with the average velocities shown in Figure 4.

For the reservoir interval we make use of a comprehensive suite of logs in well CFU 28-1, as described in Ditkof (2013). The porosity log indicates a relatively constant value of 23% over most of the 16-m reservoir interval. The mineral composition logs detail the volume fraction of quartz, clay, and calcium, roughly 0.60%, 0.17%, and 0.00%, respectively. Fluid logging estimates of the saturations agree with the analysis of cores from the well, indicating a saline water saturation of around 75%, an oil saturation of 25%, and negligible gas prior to starting the EOR operation. In Table 1 we give the properties of the four main fluids, brine, oil, methane, and carbon dioxide, at reservoir conditions, a temperature of 13 ° C and a pressure of 32 MPa (Ditkof et al., 2013). The hydrocarbon phase within the D-E sandstone unit of the Lower Tuscaloosa is an oil with an API number of 39° (Ditkof, 2013, p. 24). As indicated in Figures 10 and 11, the oil contains dissolved methane, which will alter its density, bulk modulus, and viscosity. We use the relationships in Batzle and Wang (1992) to account for the effect of the gas in solution, using an average value for the fraction of methane, and the average reservoir pressure and temperature. The values in Table 1 were used to compute the upper and lower bounds on the velocity changes provided by the Voigt and Reuss averages of the fluid moduli. Similarly, using the mineral composition log data, we can form a volume weighted average to estimate the grain density ρ_{grain} of the reservoir material using

$$\rho_{grain} = V_{quartz} \cdot \rho_{quartz} + V_{clay} \cdot \rho_{clay} \quad (27)$$

where V_{quartz} and V_{clay} are the volume fractions of the quartz and clay and ρ_{quartz} and ρ_{clay} are the respective densities. Thus, we can estimate ρ_{sat} using equation 10. There were both compressional and shear sonic logs within the reservoir interval in well CFU 28-1, though the shear sonic log did not extend

up into the overburden. These sonic logs provide V_p^{sat}, the compressional velocity of the saturated rock, and V_s^{sat} the shear velocity of the saturated rock. Using equation 11 and the fact that the shear velocity V_s^{sat} is given by

$$V_s^{sat} = \sqrt{\frac{G_{sat}}{\rho_{sat}}}, \quad (28)$$

we can estimate both G_{sat} and K_{sat}. Recall that the presence of the fluids does not change the shear modulus and we have $G_u = G_{sat}$. With the remaining log information we can use equation 9 to solve for K_u. The values of G_u and K_u that we determined in this way are given in Table 1. Using the fluid saturations, and the properties of the fluids, we calculate the composite fluid density ρ_{fluid}, using equation 13.

Table 1
Reservoir Properties for the Properties of the Effective Solid Matrix and the Four Reservoir Fluids

Category	Parameter	Description (units)	Value
Solid	K_s	Grain bulk modulus (Pa)	34.00×10^9
	G_u	Grain shear modulus (Pa)	35.00×10^9
	ρ_s	Grain density (kg/m^3)	2587.00
	K_u	Frame bulk modulus (Pa)	6.20×10^9
	G_u	Frame shear modulus (Pa)	7.13×10^9
Fluids	K_j	Bulk modulus (Pa)	2.86×10^9 (Brine) 0.13×10^9 (CO_2) 0.21×10^9 (Methane) 0.57×10^9 (Oil)
	ρ_j	Density (kg/m^3)	1060.00 (Brine) 660.00 (CO_2) 180.00 (Methane) 762.00 (Oil)
	μ_j	Viscosity (Pa-s)	1.00×10^{-3} (Brine) 0.50×10^{-4} (CO_2) 0.50×10^{-4} (Methane) 1.44×10^{-3} (Oil)

For the compositional estimate for the four fluid components, brine, oil, carbon dioxide, and methane, given by equation 25, the fluid pressure variations in Figure 9 were used to compute spatially varying moduli for the fluids. The pressure-dependent properties, in particular the densities, bulk moduli, and viscosities for water, carbon dioxide, and methane were obtained from the National Institute of Standards tables provided by Lemmon et al. (2005). The dissolved solid content of the brine was based upon two fluid samples from well CFU 29-12 measuring an average of 143,000 mg/L, primarily NaCl. The effects of the salinity on the density and bulk modulus, as functions of reservoir pressure and temperature, were modeled using the cubic regressions of Batzle and Wang (1992). The oil phase was characterized by an API value of 39° (Ditkof, 2013), and the pressure, temperature, and gas content dependent properties were estimated using the relationships presented by Batzle and Wang (1992). The relative permeability curves of Weaver and Anderson (1966), with modifications made in order to match the monthly production data and CO_2 breakthrough times (Alfi & Hosseini, 2016), were used in the computation of the dynamic permeability, as described in Vasco (2013).

Having determined the values of all the necessary parameters, we use equations 9 and 25 to estimate the impact of the saturation distributions at the time of the baseline and monitor seismic surveys, shown in Figures 10 and 11, on the seismic velocities. This is necessarily a crude estimate that ignores the heterogeneity within the reservoir and is forced upon us because we cannot resolve the detailed structure from the data at hand. However, the estimates allow us to map the pressure variations in Figure 9, along with the saturation changes in Figures 10 and 11, into rough estimates of the velocity changes and ultimately into seismic amplitude changes and time shifts. We can then compare the calculated time-lapse changes to the observations and attempt to find correspondences between the two sets of values. The unmodeled heterogeneity will show up as additional spatial variations within the data.

As a prelude to the presentation of our results, we consider the variations in compressional velocity as functions of water, total gas, and oil saturations. This will facilitate our interpretation of the calculated time-lapse changes presented below. Figure 12 is an example of the variation in compressional velocity as a function of the saturations of the fluid phases. The calculation is based upon equations 9, 10, 11, and 13, where we have used the reservoir parameters obtained from well CFU 28-1. For the composite fluid bulk modulus we employ the Reuss average, given by equation 14, as this is appropriate for well mixed fluids or fluids that are distributed in layers perpendicular to the direction of the propagating seismic wave. For seismic frequencies and layers that are nearly horizontal, this is an acceptable approximation. For this illustration, we consider the gas to be composed entirely of carbon dioxide. Note how the velocity decreases precipitously as the gas saturation increases to just a few percent.

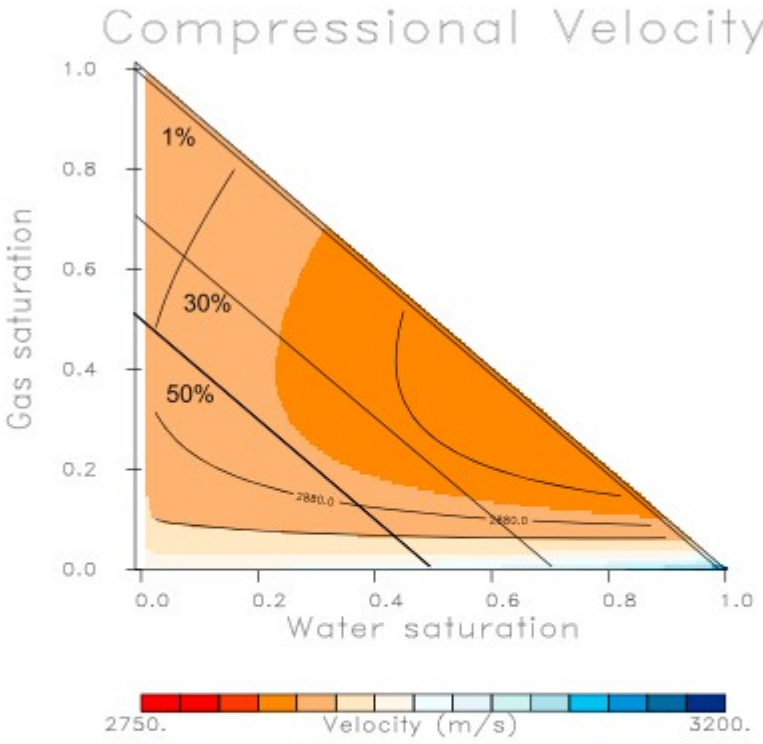

Figure 12. A triangular plot of compressional wave velocity variations as a function of water, carbon dioxide, and oil saturations, calculated using fluid substitution techniques including Gassmann's equation and the Reuss average for K_{fluid}. Because the saturations must sum to 1, the oil saturation is given by $S_o = 1 - S_w - S_g$, where S_o is the oil saturation, S_w is the water saturation, and S_g is the gas saturation. Hence, the oil saturation along the diagonal of the triangle is 0, and the oil saturation at the origin is 1.

Another important feature of Figure 12 is the decrease in velocity change with increasing oil saturation. This aspect is hard to discern because it is concentrated at the lower edge of the saturation triangle, where the gas saturation is nearly zero. In order to see this effect more clearly, consider the slices parallel to the diagonal of the saturation triangle, but intersecting different locations on the horizontal axis denoting water saturation (Figures 12 and 13). We only plot an increase of up to 5% in carbon dioxide saturation, with varying oil saturations of 1%, 30%, and 50%. We observe large variations in the magnitude of the velocity decrease with increasing carbon dioxide, depending upon how much oil is present within the pores (Figure 13). In particular, in the presence of 1% oil there is a velocity decrease of about 275 m/s as the fraction of carbon dioxide increases from 0 to 5%. If the oil within the pores increases to 30%, then the decrease in velocity with carbon dioxide fraction is reduced to about half of that value. At an oil saturation of 50% the decrease in velocity is reduced to around 70 m/s. Thus, the presence of oil in the pores can have a significant impact on how much the velocity changes with the introduction of carbon dioxide. In a

similar fashion, concentrations of methane can also reduce the velocity reductions that would be expected due to the injection of CO_2 into a water-saturated medium.

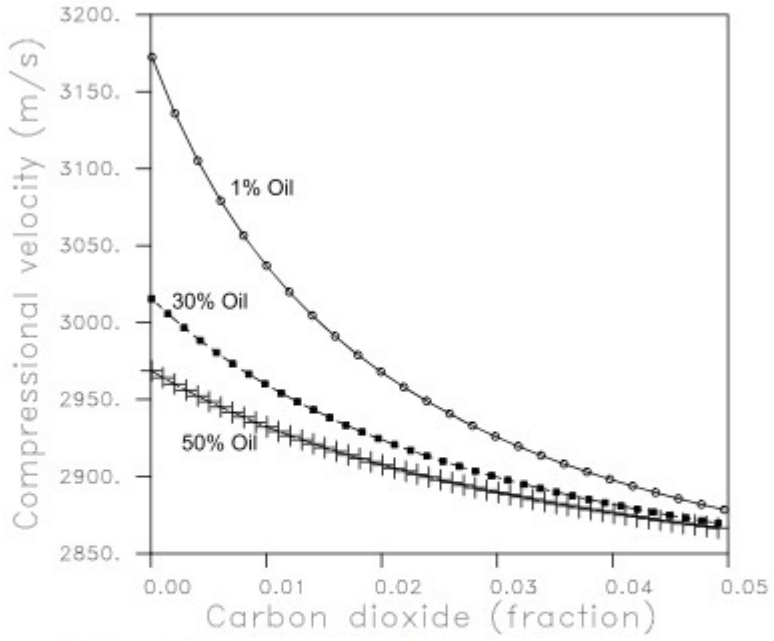

Figure 13. The variation in compressional velocity as a function of carbon dioxide saturation. As in Figure 12, the system contains oil, water, and carbon dioxide but no methane. Each curve is for a different background oil saturation that does not change. The curves may be thought of as cross-sections through the triangle in Figure 12 that are parallel to the diagonal.

Using the average fluid pressure and the saturations from the multicomponent reservoir simulation (Figures 9-11), and the rock physics techniques described above, we can estimate the seismic velocities at the times of the seismic baseline and monitor surveys as well as the seismic velocity changes. In order to account for the possible variations in fluid distributions, we shall use both the Reuss and Voigt approaches, given by equations 14 and 15, to compute composite fluid moduli, denoted by K_{Reuss} and K_{Voigt}, respectively. Mapping the fluid saturations into a composite modulus (K_{fluid}) and density (ρ_{fluid}), and then using equations 9-11 to calculate the compressional velocity for each location in the reservoir model, we can difference the velocity estimates at the times of the baseline and monitor surveys to calculate the velocity changes, shown in Figure 14. In addition, we calculated the velocity changes using the more comprehensive extension of Biot theory, given by equation 25. This estimate accounts for the variations in the four main fluid components, water, oil, carbon dioxide, and methane, and the changes in the fluid properties as a function of the spatially varying reservoir fluid pressure. These values are plotted in the central panel of

Figure 14, under the label “Four Fluids.” As expected, these values are bounded above and below by the Voigt and Reuss estimates.

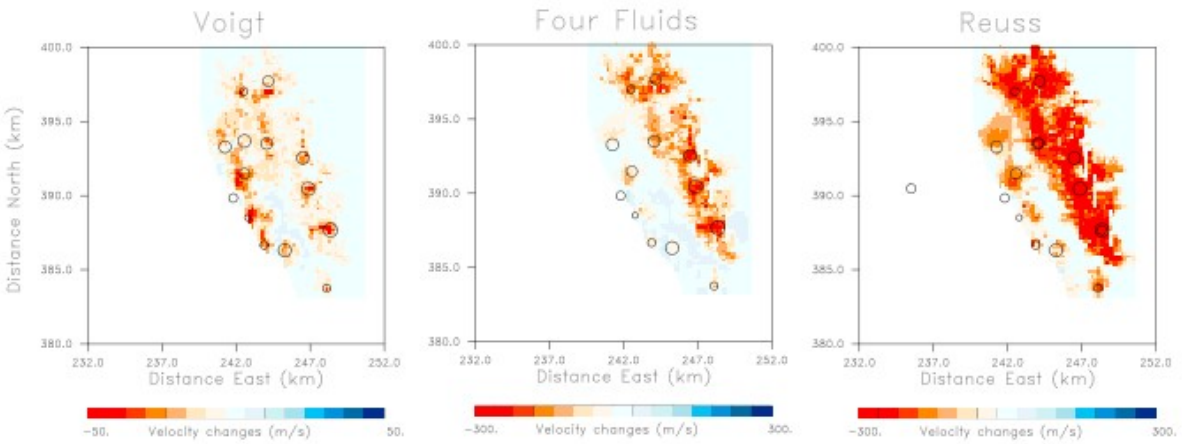

Figure 14. Calculated compressional wave velocity changes calculated using Gassmann's equation and the Voigt and Reuss different averaging techniques to compute lower and upper bounds on the fluid bulk modulus K_{fluid}.Note that the scale is different for the velocity based upon the Voigt average. The saturation distributions in Figures 10 and 11 were used in the calculations, as were the properties of the reservoir estimated from the logs at well CFU 28-1. In addition, an extension of Biot, (1956a, 1956b) theory, described in the appendix, is used to estimate velocity variations due to changes in four fluid phases (brine, oil, carbon dioxide, and methane).The properties of the fluids vary spatially in response to changes in the average fluid pressure throughout the reservoir, as shown in Figure 9.

In general, the velocity decreases occur in the areas that saw increases in total gas content from 2008 to 2010, primarily due to the injection of carbon dioxide. There are two main regions where carbon dioxide increased substantially. One area is defined by a line of wells that roughly parallels the bounding fault that constitutes the western edge of the reservoir model. The other larger area follows a subparallel track of wells extending down into the aquifer, to the east of the remaining oil rim. Note how the relative magnitudes of the velocity changes in the two regions depends upon the technique used to average the fluid moduli into a composite modulus. Specifically, if the Reuss average is used, then the largest changes are observed in the aquifer, while if the Voigt average is the basis for calculating K_{fluid}, then the largest changes are near the bounding fault. Also note that the magnitude of the velocity changes associated with the Voigt average are much smaller, around 50 m/s, than the other two estimates. The four fluid estimates of the velocity changes, resulting from the solution of equation 25, are between the two end-member models; however, the largest changes are in the aquifer, similar to the distribution associated with the Reuss average. Even with these differences, there are common features in all of the estimates. All of the velocity changes produce two subparallel regions of velocity change that appear to converge at their northern edge.

The computation of the synthetic seismograms associated with the baseline and monitor velocity models is based upon a partial expansion of reverberation operators derived by Kennett, (1974, 1983, p. 217). The approach allows for reflections at nonzero offsets, internal multiples, and

tuning effects within the reservoir interval. In calculating the reflection amplitudes, we are invoking a locally plane layered approximation and vertically propagating plane waves. The approach has been used for time-lapse imaging of saturation changes and the estimation of flow properties (Vasco et al., 2004). Here we use the saturation changes to calculate the velocities in the reservoir and then include them in our average elastic model (see Figure 4).

We calculate the amplitudes of the reflected waves at the top of the reservoir for the saturation distributions at the time of the baseline and monitor surveys. Differencing these amplitudes produces a prediction of the time-lapse changes due to the EOR processes that may be compared to the observed changes plotted in Figure 6. However, before this comparison we need to account for differences due to the variations in source size, receiver sensitivity, near surface velocity variations, and other factors that are difficult to determine and model accurately. To minimize the influence of these factors and facilitate a comparison, we normalize the differences by the average amplitude of the baseline and monitor surveys, for the *i*th trace we have

$$\overline{\delta A_i(t)} = \frac{M_i(t) - B_i(t)}{M_i(t) + B_i(t)}, \quad (29)$$

where $B_i(t)$ and $M_i(t)$ are the amplitude estimates of *i*th traces of the baseline and monitor surveys.

In Figure 15 we plot the normalized time-lapse amplitude changes for reflections from the top of the reservoir as a percentage change. Both the Voigt and Reuss estimates are shown, as are the amplitude changes predicted by the extension of Biot theory to a medium containing four fluids. The two areas noted previously are evident as amplitude decreases: one near the bounding fault and the other surrounding the wells injecting CO_2 into the aquifer. In the Reuss and compositional estimates, the region near the bounding fault has a weaker amplitude change in comparison to the aquifer area. However, this is reversed in the Voigt model, where the aquifer has a slightly weaker response. We can compare the predicted seismic amplitude changes with those extracted from the field data. For example, in Figure 16 we plot the normalized amplitude changes for the reflection off of the top of the reservoir, using the same color scale as in Figure 15. In Figure 16 we mask out changes to the west of the bounding fault as this region was not included in the reservoir model. We see considerable spatial variation in the amplitude changes, and there are significant changes far from the wells. There is an area of amplitude change adjacent to the bounding fault. Furthermore, the largest amplitude changes coincide with the location of the aquifer surrounding the easternmost line of injection wells. A region of low amplitude change lies between two areas, though they to appear to merge to the north.

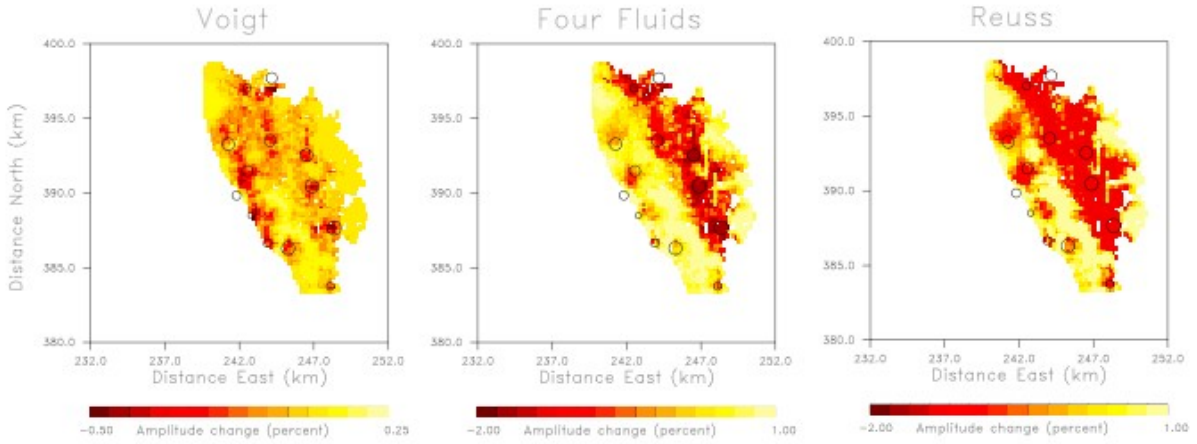

Figure 15. Amplitude changes for reflections from the top of the reservoir, based upon rock physics models that use three different techniques to calculate the fluid bulk modulus K_{fluid}. The Reuss and Voigt approaches provide the lower and upper bounds on the velocity changes, while the extension of *Biot* theory (Biot, 1956a, 1956b) to four fluid components, discussed in the appendix, provides a more comprehensive estimate of the changes due to saturation and fluid pressure changes.

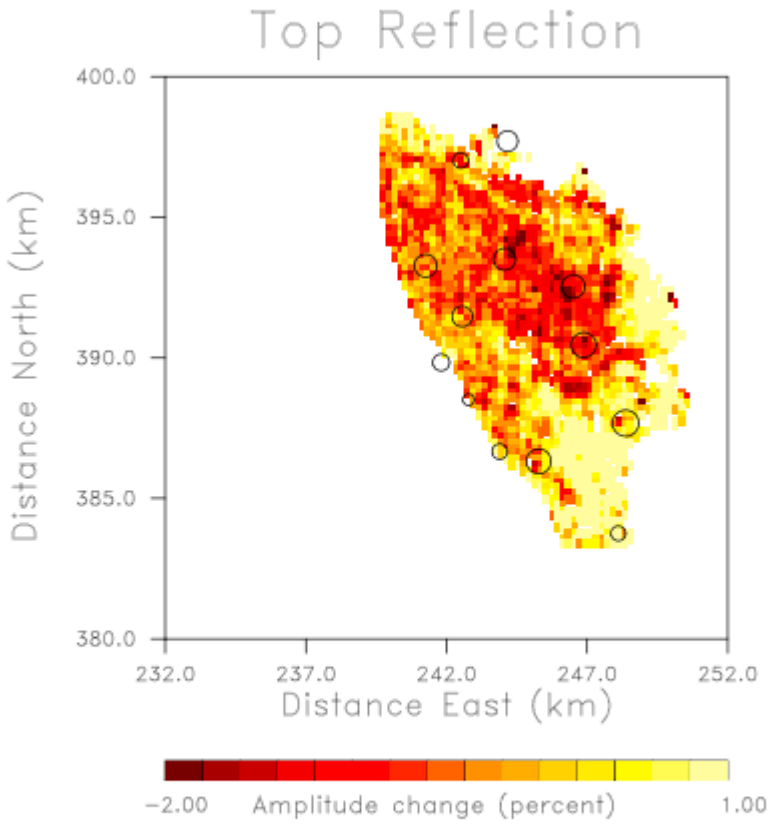

Figure 16. Estimated root mean square amplitude changes for reflections from the top of the reservoir. The open circles denote wells that actively injected carbon dioxide into the reservoir during this time.

We can also use the synthetic seismograms for the baseline and monitor surveys to calculate travel time shifts associated with reflections from just below the reservoir. Applying the CLM procedure, based upon equation 8, to the synthetic seismograms we compute the times shifts predicted by the compositional reservoir model. In Figure 17 we plot the estimated lower and upper bounds, based upon the Voigt and Reuss averages, along with values calculated using the extension of Biot theory to four fluids. The largest time shifts in Figure 17 are associated with the two lines of CO_2 injection wells, separated by area where the changes are small or negative. Note that the magnitude of the time shifts based upon the Voigt average is much smaller than both the Reuss-based and Biot-based estimates.

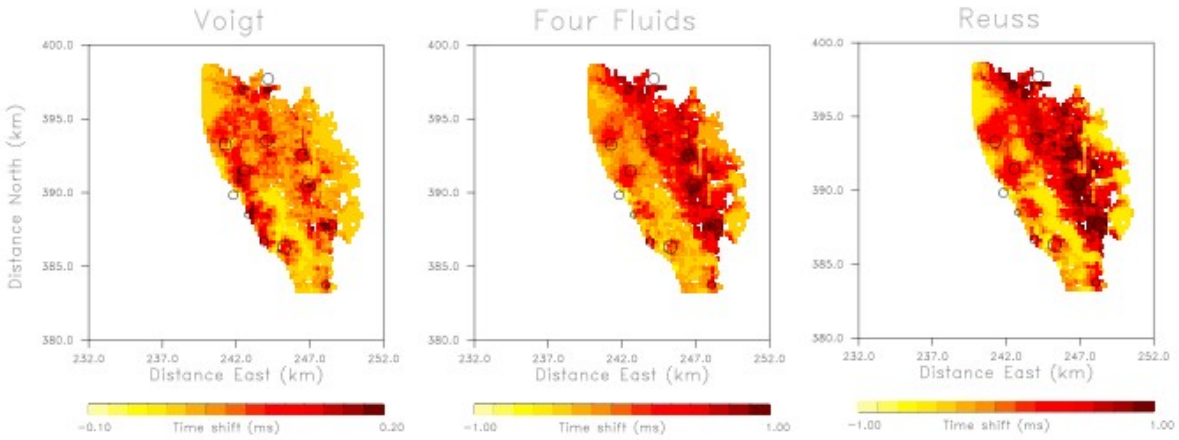

Figure 17. Time shifts calculated using the saturations shown in Figures 10 and 12 and rock physics models that use the Reuss and Voigt techniques for averaging the fluid moduli to estimate the composite fluid bulk modulus K_{fluid} and hence bounds on the travel time shifts. Travel time shifts, based upon a multicomponent modeling technique with estimates given by equation (25), are shown in the middle panel of the figure.

In Figure 18 the observed time shifts, estimated by the CLM, are shown. Though there is considerable scatter in the observed time shifts, the main features noted in the predictions from the compositional simulation are visible. For example, there are positive time shifts, associated with a lowering of the velocity, adjacent to the bounding fault. There are also positive time shifts in the region surrounding the wells that are injecting carbon dioxide into the aquifer. The trough between the two areas of positive time shifts is visible, and it shrinks to the north as the two features merge The magnitude of the observed time shifts is of the same order as the time shifts predicted using Reuss averaging and the four component compositional model, and much larger than those calculated using Voigt averaging.

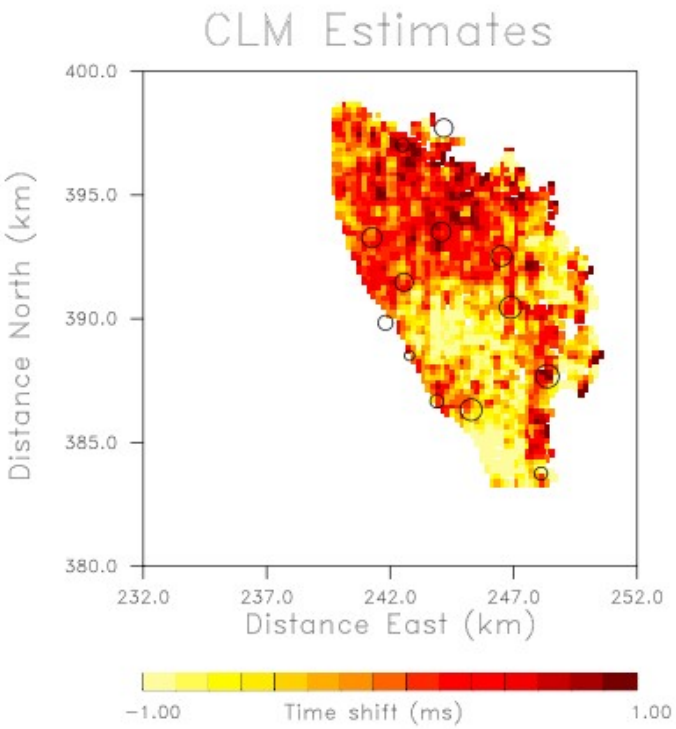

Figure 18. Estimated time shifts associated with reflections from interfaces just below the reservoir, extracted using the correlation leakage method (CLM) of Whitcombe et al. (2010).

5 Discussion

Using the time-lapse seismic observations gathered over the oil field at Cranfield, Mississippi, we have extracted amplitude changes for reflections from the top of the reservoir and time shifts for waves passing through the reservoir. Both of these sets of observations contain considerable spatial variability, most likely due to the significant reservoir heterogeneity and inherent noise in the data. Reservoir heterogeneity is to be expected as the D-E sandstone unit of the lower Tuscaloosa Formation is composed of numerous sandstone bodies representing point bars and meandering stream channels along with variable conglomerates and stringer sands. The detailed reservoir model contains some elements of this heterogeneity due the stochastic algorithm used to generate the model for history matching. However, it is difficult or impossible to fully characterize the spatial variations in reservoir properties with surface seismic observations, given the frequency content and the spatial averaging of such data.

Upon conducting a full simulation of the history of the field some regularity becomes evident, due to the large-scale fluid distribution within the reservoir. In particular, we note sizable amplitude changes and time shifts associated with wells adjacent to the fault defining the western edge of the reservoir model. An additional region of notable amplitude changes and time shifts lies to the east where a line of wells are injecting carbon dioxide directly into the aquifer, adjacent to the remains of the oil ring within the

anticline. Rock physics modeling, based upon Gassmann's equation and an extension of Biot theory to four fluids, indicates that injecting carbon dioxide into fully water saturated sediments can produce a large seismic response and that response is significantly reduced in the presence of oil (Figures 12 and 13). This would explain why the amplitude changes and time shifts within the aquifer are large and extend far from the injection wells, into regions with moderate or even small concentrations of CO_2.

The time-lapse observations share the general characteristics of the predictions made by the simulation models. However, there are differences between the patterns of observed and predicted changes, and differences between the changes in reflection amplitudes and time shifts. For example, the observed amplitude changes in the aquifer do not fully extend to southern edge of the grid, as they do in the predicted changes and in the observed time shifts. Furthermore, there is considerable scatter in the estimated time shifts in Figure 18. There are several factors that could contribute to these differences. First, the reservoir model is based upon field-wide data and is likely to differ from the actual structure of the reservoir, particularly at scales smaller then the spacing of the wells. Second, the elastic model is very simple, and the vertical and lateral heterogeneity of the reservoir is not known or accounted for. Third, the top reflection amplitude is sensitive to properties of the formation just above the reservoir and more sensitive to the upper portion of the reservoir. Therefore, changes at the base of the reservoir may not result in a significant change in the amplitude. In contrast, the time shifts for reflections from layers below the reservoir are equally sensitive to changes throughout the reservoir interval. Fourth, the analysis assumes vertically propagating waves and a locally layered structure. The stacking process will introduce contributions from larger offsets and at wider reflection angles. It has been shown that techniques for estimating time shifts work best on zero-offset prestack data and that migration and stacking introduce considerable noise (Kanu et al., 2016). Finally, there are different approaches for defining the seismic amplitude changes, depending on parameters such as the window length used in calculating the root mean square amplitude, and the estimated amplitude changes can and do vary between studies (Alfi et al., 2019; Carter, 2014; Ditkof, 2013; Zhang et al., 2014).

The results of this study reflect some of the limitations that are common in the setting of an operating petroleum reservoir. There are few wells that contain sonic logs in the overburden, only three wells had compressional wave data and just one had shear information gathered for some distance above the reservoir. The lack of well data precluded the construction of a detailed elastic model for the overburden and the reservoir. Such a model would be useful in accounting for some of the reservoir heterogeneity. Aspects of the time-lapse surveys also impacted our efforts to image the changes associated with the injection of carbon dioxide. Our analysis of seismic amplitudes and time shifts was based upon poststack seismic data,

and the results might improve significantly through the direct use of pre-stack, near-offset observations. The edge of the survey was close to the study area, leading to low fold and greater noise in the seismic data.

Due to the limitations noted above, several simplifying assumptions were adopted in this study. Because it was not possible to characterize the heterogeneity in sufficient detail, it was necessary to consider saturations and pressures averaged over the roughly 20-m thickness of the reservoir. Furthermore, the overburden velocity model was essentially one dimensional. Any deviations from these assumptions will appear as unmodeled variations in the amplitude changes and time shifts in Figures 16 and 18. Though we allowed for spatial variations in pore pressure when calculating the fluid properties, pressure-induced geomechanical effects were neglected. While there is some evidence of geomechanical effects at the Cranfield site (Kim & Hosseini, 2013), the observed velocity changes due to pressure variations are relatively small (Marchesini et al., 2017), less than 1%, leading to a roughly 0.1-ms change in the two-way travel time through the reservoir. Finally, chemical reactions due to the introduction of carbon dioxide into the reservoir were not accounted for. However, such reactions are thought to play a minor role at the Cranfield site (Lu et al., 2012b).

6 Conclusions

Observed seismic time-lapse amplitude changes and time shifts are compatible with predictions based upon a multicomponent reservoir simulation. In particular, velocity changes due to the injection of carbon dioxide into the aquifer leg of the reservoir lead to large and widespread changes in seismic amplitudes and substantial time shifts for waves that propagate across the reservoir. Rock physics modeling points to the influence of the in situ oil content on the sensitivity of seismic velocity to changes in the saturation of carbon dioxide. This result agrees with previous suggestions that the presence of oil can depress seismic velocity changes due to the injection of carbon dioxide (Ditkof, 2013).

The results imply that onshore seismic time-lapse data can be used to image large-scale velocity changes due to the geological storage of carbon dioxide. However, without adequate constraints on reservoir properties it can be difficult to make quantitative estimates of stored volumes. The difficulties are exacerbated during enhanced oil production where the pore fluid distribution can be quite complex, and it is not clear how to average fluid moduli when calculating seismic velocities. At Cranfield, it seems that the Reuss average and the extension of Biot theory to four fluid components appear to match the magnitudes of the observed time-lapse amplitude and travel time changes while the Voigt average does not.

Acknowledgments

We thank Denbury Onshore LLC for hosting the work reported in this study at their Cranfield site. The development of the technique for the calculation of

seismic velocities in a medium containing N_f fluids was supported by the U.S. Department of Energy, Office of Science, Office of Basic Energy Sciences, Chemical Sciences, Geosciences, and Biosciences Division under contract DE-AC02-05- CH11231. The analysis of the Cranfield data performed at Lawrence Berkeley National Laboratory was supported by the U.S. Department of Energy under contracts DE-FC26-05NT42590 and DE-AC02-05- CH11231, Assistant Secretary for Fossil Energy, Office of Coal and Power Systems through the National Energy Technology Laboratory. The Southeast Regional Carbon Sequestration partnership (SECARB) project is managed by the Southern States Energy Board, Kenneth Nemeth PI. The reflection amplitude changes, the time shifts, and the saturations from the reservoir modeling are publically available on the Zenodo respository via the identifier doi:10.5281/zenodo.1328298.

Appendix A: Elastic Velocities for a Porelastic Medium Containing N_f Fluids

In this appendix we generalize the three-phase work of Vasco (2013) to allow for N_f fluid components. We begin with an extended set of equations, given in the frequency domain, governing the evolution of the solid $U(x,\omega)$ and fluid $W_i(x,\omega)$, $i=1,2,\ldots,N_f$ displacements. As in the case of a single phase, the presence of the fluids will influence the response of a porous body to imposed stresses. The porous elastic solid is characterized by the porosity φ. However, the pores may be filled with some combination of N_f fluids, and we will denote the saturation (fraction) of the nth fluid by S_n. Because the pore is taken to be fluid filled, the saturations sum to unity

$$\sum_{n=1}^{N_f} S_i = S_1 + S_2 + \cdots + S_{N_f} = 1. \quad \text{(A1)}$$

It will be convenient to denote the fraction of a given unit volume of material for the solid

$$\alpha_s = (1-\varphi) \quad \text{(A2)}$$

and for the N_f fluids

$$\alpha_n = \varphi S_n, \quad \text{(A3)}$$

The presence of multiple fluids introduces several complications. The chief difficulty is that it renders the problem nonlinear, because the evolution of the saturation is severely impacted by the current saturated state. That is, due to the ability of one fluid to block the flow of another, the fractional flow of the fluid will depend upon the existing saturations. For the case considered here, the passage of an elastic wave, we linearize the problem by assuming that the saturation changes induced by the wave are small. Following the approach taken in Vasco (2013) and Vasco and Datta-Gupta (2016), suitably generalized for the case of N_f fluids, one can produce N_f+1 governing equations, where the first equation is indexed by $n=1,2,\ldots,N_f$ and actually represents N_f equations:

$$\nu_n \mathbf{U} + \Gamma_n \mathbf{W}_n = \nabla \left[C_{ns} \nabla \cdot \mathbf{U} + \sum_{j=1}^{N_f} M_{nj} \nabla \cdot \mathbf{W}_n \right]$$

$$\nu_s \mathbf{U} + \sum_{j=1}^{N_f} \xi_j \mathbf{W}_j = \nabla \left[K_u \nabla \cdot \mathbf{U} + \sum_{j=1}^{N_f} C_{sj} \nabla \cdot \mathbf{W}_j \right] + \nabla \cdot \boldsymbol{\tau}, \quad \text{(A4)}$$

where τ is the deviatoric stress, given by

$$\boldsymbol{\tau} = G \left[\nabla \mathbf{U} + \nabla (\mathbf{U})^T - \frac{2}{3} \nabla \cdot \mathbf{U} \mathbf{I} \right] \quad \text{(A5)}$$

for a solid matrix with shear modulus G. The poroelastic parameters K_u (undrainded bulk modulus), C_{ns} and C_{sj} (Biot coupling moduli), and M_{nj} (fluid storage coefficients) are the multicomponent fluid equivalents to the single-phase constants, as given in Wang (2000) and Pride (2005). To keep the equations in a compact form, we have defined the additional coefficients

$$\nu_s = \alpha_s \rho_s \omega^2, \quad \text{(A6)}$$

$$\nu_n = \alpha_n \rho_n \omega^2, \quad \text{(A7)}$$

$$\xi_j = \alpha_j \rho_j \frac{\mu_j}{k_j(\omega)} \omega, \quad \text{(A8)}$$

$$\Gamma_n = \alpha_n \rho_n \left[\omega - \frac{\mu_n}{k_n(\omega)} \right] \omega, \quad \text{(A9)}$$

where ρ_s is the solid density, ρ_n is the density of the nth fluid, μ_n is the viscosity of the nth fluid, and $k_n(\omega)$ is the dynamic permeability discussed in Johnson (1987), Pride (2005), and Vasco and Datta-Gupta, (2016, p. 82), associated with the nth fluid. As derived in Johnson (1987), and explained in Vasco and Datta-Gupta (2016, p. 82), one can develop an expression for $k_n(\omega)$ of the form

$$\frac{1}{k_n(\omega)} = \frac{1}{k_o} \left[\sqrt{1 - i \frac{\omega}{\omega_n} \Pi} - i \frac{\omega}{\omega_n} \right], \quad \text{(A10)}$$

where

$$\Pi = 4 \frac{\nu_\infty k_o}{\Lambda^2 \varphi} \quad \text{(A11)}$$

is a pore geometry term containing the tortuosity in the limit of high frequency v_∞, the static permeability k_o used in fluid flow modeling, and Λ, which is twice the ratio of the weighted pore volume to the weighted surface area. The parameter ω_n is the crossover frequency for the nth fluid

$$\omega_n = \frac{\mu_n \varphi}{\rho_n \nu_\infty k_o}, \quad \text{(A12)}$$

signifying the transition from viscous dominated flow to that dominated by inertial forces.

As shown in Vasco (2013) and Vasco and Datta-Gupta (2016, p. 291), for a reservoir with smoothly varying properties, we may derive an asymptotic solution in terms of the ratio of the seismic wavelength to the length scale of the spatial variations in material and fluid properties, ε, in the form of a propagating wave

$$\mathbf{U}(\mathbf{x},\omega) = e^{j\theta}\sum_{l=0}^{\infty}\varepsilon^{l}\mathbf{U}_{l}(\mathbf{x},\omega), \quad \text{(A13)}$$

where $\theta(x,\omega)$ is the phase and U_l is successive higher-order amplitude corrections. Similar expansions also hold for the fluid displacements $W_n(x,\omega)$. Substituting the series representations into the governing equations A4, and restricting our attention to the lowest, zeroth-order terms in l, transforms them into the linear system

$$\Omega\mathbf{V}_{o} = \mathbf{0}, \quad \text{(A14)}$$

where V_o is a vector of the zeroth-order amplitudes. The matrix Ω is given by the $3(N_f+1) \times 3(N_f+1)$ coefficient array

$$\begin{bmatrix} \alpha\mathbf{I}-\beta\mathbf{p}\mathbf{p}^{T} & \xi_1\mathbf{I}-C_{s1}\mathbf{p}\mathbf{p}^{T} & \cdots & \xi_{N_f}\mathbf{I}-C_{sN_f}\mathbf{p}\mathbf{p}^{T} \\ \nu_1\mathbf{I}-C_{1s}\mathbf{p}\mathbf{p}^{T} & \Gamma_1\mathbf{I}-M_{11}\mathbf{p}\mathbf{p}^{T} & \cdots & -M_{1N_f}\mathbf{p}\mathbf{p}^{T} \\ \vdots & \vdots & \ddots & \vdots \\ \nu_{N_f}\mathbf{I}-C_{N_f s}\mathbf{p}\mathbf{p}^{T} & -M_{N_f 1}\mathbf{p}\mathbf{p}^{T} & \cdots & \Gamma_{N_f}\mathbf{I}-M_{N_f N_f}\mathbf{p}\mathbf{p}^{T} \end{bmatrix}. \quad \text{(A15)}$$

The vector p is the gradient of the phase, $\nabla\theta$. For brevity, we have defined the coefficients

$$\alpha = \nu_s - Gp^2, \quad \text{(A16)}$$

$$\beta = K_u + \frac{1}{3}G \quad \text{(A17)}$$

in equation A15. The linear system of equations A14 will have a nontrivial solution V_o if the determinant of the coefficient matrix Ω vanishes (Noble & Daniel, 1977, p. 203). The requirement that the determinant of Ω vanishes leads to a polynomial equation in the components of the phase gradient vector p, also known as the slowness vector. Because $p=\nabla\theta$, the resulting polynomial equation is a differential equation for the function $\theta(x,\omega)$, an extension of the eikonal equation to a poroelastic medium contain N_f fluids. Computing the determinant of the full matrix Ω directly leads to some very complicated algebra, something that we will work to avoid.

Because the determinant of a matrix is equal to the product of the matrix eigenvalues, the require that $\det\Omega = 0$ is equivalent to the vanishing of one of the eigenvalues, λ,

$$\Omega\mathbf{e} = \lambda\mathbf{e} = \mathbf{0}, \quad \text{(A18)}$$

where e is the corresponding eigenvector. In and of itself, equation A18 does not reduce the algebraic burden, as it is equivalent to equation A14. However, we can invoke some mathematical and physical arguments for a

particular form for the eigenvector e that leads to the determinant of a reduced system of equations. In particular, note that the matrix Ω is composed of $(N_f+1)\times(N_f+1)$ block matrices, each of which is in the form of a linear combination of the identity matrix I and the dyadic matrix $\mathbf{p}\mathbf{p}^T$. Therefore, we might suspect that candidate eigenvectors might be composed of vectors parallel to p

$$\mathbf{e}^{l} = \begin{bmatrix} y\mathbf{p} \\ y_1\mathbf{p} \\ \vdots \\ y_{N_f}\mathbf{p} \end{bmatrix}, \quad \text{(A19)}$$

where y and y_i are scalar coefficients, or of vectors perpendicular to p

$$\mathbf{e}^{\perp} = \begin{bmatrix} s\mathbf{p}^{\perp} \\ s_1\mathbf{p}^{\perp} \\ \vdots \\ s_{N_f}\mathbf{p}^{\perp} \end{bmatrix} \quad \text{(A20)}$$

because the multiplication of the vectors p or $\mathbf{p}^{\perp}$ by linear combinations of I and $\mathbf{p}\mathbf{p}^T$ returns the same vector, scaled by some factor.

Physical considerations also suggest eigenvectors in the form of $\mathbf{e}^{l}$ and $\mathbf{e}^{\perp}$. For example, Pride (2005) has shown that in a homogeneous medium, nontrival solutions to the equations of poroelasticity only exist when the vectors U and W are in the same direction. Furthermore, using potentials, one can show that in a homogeneous poroelastic medium, propagating waves decouple into longitudinal modes parallel to p, and transverse modes in the direction of $\mathbf{p}^{\perp}$. Thus, the candidate eigenvector (A19) represents particle motion in the direction of propagation and a compressional mode. The vector (A20), on the other hand, produces particle motion transverse to the direction of motion and a shear wave. Because $\mathbf{p}^{\perp}$ lies in the plane perpendicular to p, there is some freedom in defining this direction.

In the application to the Cranfield time-lapse data we shall be interested in the longitudinal mode of propagation. Therefore, we consider the eigenvalue problem

$$\Omega\mathbf{e}^{l} = \mathbf{0} \quad \text{(A21)}$$

which, as shown in Vasco (2013) and Vasco and Datta-Gupta (2016), is equivalent to the highly structured form

$$[\mathbf{M} \otimes \mathbf{I}]\,\mathbf{e}^{l} = \mathbf{0}, \quad \text{(A22)}$$

where M⊗I signifies the tensor product of the two matrices M and I

$$\mathbf{M} \otimes \mathbf{I} = \begin{bmatrix} m_{11}\mathbf{I} & m_{12}\mathbf{I} & \dots & m_{1(N_f+1)}\mathbf{I} \\ m_{21}\mathbf{I} & m_{22}\mathbf{I} & \dots & m_{2(N_f+1)}\mathbf{I} \\ \vdots & \vdots & \ddots & \vdots \\ m_{(N_f+1)1}\mathbf{I} & m_{(N_f+1)2}\mathbf{I} & \dots & m_{(N_f+1)(N_f+1)}\mathbf{I} \end{bmatrix} \quad \text{(A23)}$$

and m_{ij} is the coefficients of the coefficient matrix M

$$\mathbf{M} = \begin{bmatrix} v_s - Hs & \xi_1 - C_{s1}s & \dots & \xi_{N_f} - C_{sN_f}s \\ v_1 - C_{1s}s & \Gamma_1 - M_{11}s & \dots & -M_{1N_f}s \\ \vdots & \vdots & \ddots & \vdots \\ v_{N_f} - C_{N_f s}s & -M_{N_f 1}s & \dots & \Gamma_{N_f} - M_{N_f N_f}s \end{bmatrix}, \quad \text{(A24)}$$

where $s=p^2$ and $H=K_u+4/3G$. The exact form of the matrix M follows from the coefficient matrix in A15. For matrices in the form of a tensor product we may use the result of Silvester (2000) to write its determinant as

$$\det(\boldsymbol{\Omega}) = \det(\mathbf{M} \otimes \mathbf{I}) = \det(\mathbf{M}) \det(\mathbf{I})^{(N_f+1)} = \det(\mathbf{M}), \quad \text{(A25)}$$

The determinant of M is a polynomial of degree N_f+1 in $s=p^2$

$$Q_{(N_f+1)}s^{(N_f+1)} + Q_{N_f}s^{N_f} + \dots + Q_1 s + Q_0 = 0 \quad \text{(A26)}$$

that has N_f+1 complex roots in general. Vasco (2013) has shown how to use the multilinearity of the determinant to derive explicit expressions for the coefficients $Q_0, Q_1, \dots, Q_{(N_f+1)}$ in terms of the elements of the array M. The roots provide estimates of the magnitude of the slowness vector and thus the phase velocity of the propagating fast and slow waves in the poroelastic medium, given by

$$c = \frac{\omega}{p}. \quad \text{(A27)}$$

The smallest root provides an estimate of the highest velocity longitudinal wave, corresponding to the elastic compressional wave in the porous medium. The lower velocity waves are associated with the various slow waves that propagate within the medium and are due to capillary pressure differences between the fluids (Tuncay & Corapcioglu, 1997).

References

Ajo-Franklin, J. B., Peterson, J., Doetsch, J., & Daley, T. M. (2013). High-resolution characterization of a CO_2 plume using crosswell seismic tomography: Cranfield, MS, USA. *International Journal of Greenhouse Gas Control*, 18, 497– 509. https://doi.org/10.1016/j.ijggc.2012.12.018

Aki, K., & Richards, P. G. (1980). *Quantitative seismology*. San Francisco: W. H Freeman and Company.

Alfi, M., & Hosseini, S. A. (2016). Integration of reservoir simulation, history matching, and 4D seismic for CO_2-EOR and storage at Cranfield, Mississippi, USA. *Fuel*, 175, 116– 128. https://doi.org/10.1016/j.fuel.2016.02.032

Alfi, M., Vasco, D. W., Hosseini, S. A., Meckel, T. A., & Hovorka, S. D. (2019). Validating compositional fluid flow simulations using 4D seismic interpretation and vice versa in SECARB Early Test—A critical review. *International Journal of Greenhouse Gas Control*, 82, 162– 174. http://doi.org/10.1016/j.ijggc.2019.01.003

Arts, R., Chadwick, A., Eiken, O., Thibeau, S., & Nooner, S. (2008). Ten years experience of monitoring CO_2 injection in the Utsira Sand at Sleipner, offshore Norway. *First Break*, 26, 91– 96.

Batzle, M., & Wang, Z. (1992). Seismic properties of pore fluids. *Geophysics*, 57, 1396– 1408.

Berryman, J. G., Thigpen, L., & Chin, R. C. Y. (1988). Bulk elastic wave propagation in partially saturated porous solids. *Journal of the Acoustical Society of America*, 84, 360– 373. https://doi.org/10.1121/1.396938

Biot, M. A. (1956a). Theory of propagation of elastic waves in a fluid-saturated porous solid. Part I: Low frequency range. *Journal of the Acoustical Society of America*, 28, 168– 178. https://doi.org/10.1121/1.1908239

Biot, M. A. (1956b). Theory of propagation of elastic waves in a fluid-saturated porous solid. Part II: Higher frequency range. *Journal of the Acoustical Society of America*, 28, 179– 191. https://doi.org/10.1121/1.1908241

Boait, F., White, N. J., Bickle, M. J., Chadwick, R. A., Neufeld, J. A., & Huppert, H. E. (2012). Spatial and temporal evolution of injected CO_2 at the Sleipner Field, North Sea. *Journal of Geophysical Research*, 117, B03309. https://doi.org/10.1029/2011JB008603

Butsch, R., Brown, A. L., Bryans, B., Kolb, C., & Hovorka, S. (2013). Integration of well-based subsurface monitoring technologies: Lessons learned at SECARB study, Cranfield, MS. *International Journal of Greenhouse Gas Control*, 18, 409– 420.

Calvert, R. (2005). Insights and methods for 4D reservoir monitoring and characterization. EAGE/SEG Distinguished Instructor Short Course 8.

Carter, R. W. (2014). Fluid characterization at the Cranfield CO_2 injection site: Quantitative seismic interpretation from rock-physics modeling and seismic inversion (Ph.D. thesis), University of Texas, Austin.

Carter, R. W., & Spikes, K. T. (2013). Sensitivity analysis of Tuscaloosa sandstone to CO_2 saturation, Cranfield field, Cranfield, MS. *International Journal of Greenhouse Gas Control*, 18, 485– 496.

Carter, R. W., Spikes, K. T., & Hess, T. (2014). Inversion of multicomponent 3D vertical seismic profile data for porosity and CO_2 saturation at the Cranfield injection site, Cranfield, MS. *Interpretation*, 2, SE77– SE89. https://doi.org/10.1190/INT-2013-0147.1

Chadwick, R. A., Marchant, B. P., & Williams, G. A. (2014). CL2 storage monitoring: leakage detection and measurement in subsurface volumes from 3D seismic data at Sleipner. *Energy Procedia*, 63, 4224– 4239.

Daley, T. M., Hendrickson, J., & Queen, J. H. (2014). Monitoring CO_2 storage at Cranfield, Mississippi with time-lapse offset VSP—Using integration and modeling to reduce uncertainty. *Energy Procedia*, 63, 4240– 4248.

De, G. S., Winterstein, D. F., & Meadows, M. A. (1994). Comparison of P- and S-wave velocities and Q's from VSP and sonic log data. *Geophysics*, 59, 1512– 1529.

Delshad, M., Kong, X., Tavakoli, R., Hosseini, S. A., & Wheeler, M. F. (2013). Modeling and simulation of carbon sequestration at Cranfield incorporating new physical models. *International Journal of Greenhouse Gas Control*, 18, 463– 473. https://doi.org/10.1016/j.ijggc.2013.03.019

Ditkof, J. (2013). Time-lapse seismic monitoring for enhanced oil recovery and carbon capture and storage field site at the Cranfield Field, Mississippi (M. Sc. Thesis), University of Texas, Austin.

Ditkof, J., Caspari, E., Pevzner, R., Urosevic, M., Meckel, T. A., & Hovorka, S. A. (2013). Time-lapse seismic signal analysis for enhanced oil recovery at Cranfield CO_2 sequestration site, Cranfield Field, Mississippi. *Interpretation*, 1, T157– T166. https://doi.org/10.1190/INT-2013-0056.1

Dutta, N. C., & Ode, H. (1979). Attenuation and dispersion of compressional waves in fluid-filled porous rocks with partial gas saturation (White model) - Part I: Biot theory. *Geophysics*, 44, 789– 805.

Edwards, R. W. J., & Celia, M. A. (2018). Infrastructure to enable deployment of carbon capture, utilization, and storage in the United States. *Proceedings of the National Academy of Science*, 115, E8815– E8824. https://doi.org/10.1073/pnas.1806504115

Eiken, O. (2019). Twenty years of monitoring CO_2 injection at Sleipner. In T. L. Davis, M. Landro, & M. Wilson (Eds.), *Geophysics and Geosequestration*. Dordrecht: Springer.

Furre, A.-K., Kiaer, A., & Eiken, O. (2015). CO_2-induced seismic time shifts as Sleipner. *Interpretation*, 3, SS23– SS35. https://doi.org/10.1190/INT-2014-0225.1

Gassmann, F. (1951). Über die Elastizität poröser Medien. *Vier Der Natur*, 96, 1– 23.

Gaus, I. (2010). Role and impact of CO_2-rock interactions during CO_2 storage in sedimentary rocks. *International Journal of Greenhouse Gas Control*, 4, 73– 89.

Gibson-Poole, C. M, & Raikes, S. (2010). Enhanced understanding of CO_2 storage at Krechba from 3D seismic. In *Proceedings of the 9th Annual*

Conference on Carbon Capture and Sequestration, Pittsburgh, PA, pp. 10– 13. May 2010.

Hale, D. (2013). Dynamic warping of seismic images. *Geophysics*, 78, S105–S115. https://doi.org/10.1190/geo2012-0327.1

Hosseini, S. A., Lashgari, H., Choi, J. W., Nicot, J.-P., Lu, J., & Hovorka, S. D. (2013). Static and dynamic reservoir modeling for geological CO_2 sequestration at Cranfield, Mississippi, U.S.A. *International Journal of Greenhouse Gas Control*, 18, 449– 462. https://doi.org/10.1016/j.ijggc.2012.11.009

Hoversten, G. M., Gritto, R., Washbourne, J., & Daley, T. (2003). Pressure and fluid saturation prediction in a multicomponent reservoir using combined seismic and electromagnetic imaging. *Geophysics*, 68, 1580– 1591. https://doi.org/10.1190/1.1620632

Hovorka, S. D., Meckel, T. A., & Trevino, R. H. (2013). Monitoring a large-volume injection at Cranfield, Mississippi—Project design and recommendations. *International Journal of Greenhouse Gas Control*, 18, 345–360. https://doi.org/10.1016/j.ijggc.2013.03.021

Ivanova, A., Kashubin, A., Juhojuntti, N., Kummerow, J., Hennings, J., Juhlin, C., Luth, S., & Ivandic, M. (2012). Monitoring and volumetric estimation of injected CO_2 using 4D seismic, petrophysical data, core measurements and well logging: A case study at Ketzin, Germany. *Geophysical Prospecting*, 60, 957– 973.

Johnson, D. L. (1987). Theory of dynamic permeability and tortuosity in fluid-saturated porous media. *Journal of Fluid Mechanics*, 176, 379– 402. https://doi.org/10.1017/S0022112087000727

Johnson, D. L. (2001). Theory of frequency dependent acoustics in patchy-saturated porous media. *Journal of the Acoustical Society of America*, 110, 682– 694.

Kanu, C., Toomey, A., Hodgson, L., Gherasim, M., L'Heureux, E., Du, B., & Zhang, Q. (2016). Evaluation of time-shift extract methods on a synthetic model with 4D geomechanical changes. *The Leading Edge*, 35, 888– 893. https://doi.org/10.1190/tle35100888.1

Kennett, B. L. N. (1974). Reflections, rays, and reverberations. *Bulletin of the Seismological Society of America*, 64, 1685– 1696.

Kennett, B. L. N. (1983). *Seismic wave propagation in stratified media*. Cambridge: Cambridge University Press.

Kim, S., & Hosseini, S. A. (2013). Above-zone pressure monitoring and geomechanical analysis for a field-scale CO_2 injection project in Cranfield, MS. *Greenhouse Gases Science and Technology*, 4, 81– 98. https://doi.org/10.1002/ghg

Kordi, M. (2013). Characterization and prediction of reservoir quality in chlorite-coated sandstones: evidence from the Lat Cretaceous Lower Tuscaloosa Formation at Cranfield Field, Mississippi, U.S.A (Ph.D. Thesis), University of Texas, Austin.

Lemmon, E. W., McLinden, M. O., & Friend, D. G. (2005). Thermophysical properties of fluid systems, NIST Chemistry WebBook. NIST Standard Reference Data Base Number 69, P. J. Linstrom and W. G, Mallard ,Eds. National Institute of Standards and Technology.

Lu, J., Cook, P. J., Hosseini, S. A., Yang, C., Romanak, K. D., Zhang, T., Freifeld, B. M., Smyth, R. C., Zeng, H., & Hovorka, S. D. (2012a). Complex fluid flow revealed by monitoring CO_2 injection in a fluvial formation. *Journal of Geophysical Research*, 117, 1– 13. https://doi.org/10.1029/2011JB008939

Lu, J., Kharaka, Y. K., Thordsen, J. J., Horita, J., Karamalidis, A., Griffith, C., Hakala, J. A., Ambats, G., Cole, D. R., Phelps, T. J., Manning, M. A., Cook, P. J., & Hovorka, S. D. (2012b). Complex fluid flow revealed by monitoring CO_2 injection in a fluvial formation. *Chemical Geology*, 291, 269– 277.

Marchesini, P., Ajo-Franklin, J. B., & Daley, T. M. (2017). In situ measurement of velocity-stress sensitivity using crosswell continuous active-source seismic monitoring. *Geophysics*, 82, D319– D326. https://doi.org/10.1190/GEO2017-01061.1

Mavko, G., Mukerji, T., & Dvorkin, J. (1998). *The rock physics handbook*. Cambridge: Cambridge University Press.

Njiekak, G., Schmitt, D. R., Yam, H., & Kofman, R. S. (2013). CO_2 rock physics as part of the Weyburn-Midale geological storage project. *International Journal of Greenhouse Gas Control*, 16S, S118– S133.

Noble, B., & Daniel, J. W. (1977). *Applied linear algebra*. Englewood Cliffs: Prentice-Hall.

Norris, A. N. (1993). Low frequency dispersion and saturation in partially saturated rocks. *Journal of the Acoustical Society of America*, 94, 359– 370.

Pevzner, R., Urosevic, M., Popik, D., Shulakova, V., Tertyshnikov, K., Caspari, E., Correa, J., Dance, T., Kepic, A., Glubokovshikh, S., Ziramov, S., Gurevich, B., Singh, R., Raab, M., Watson, M., Daley, T., Robertson, M., & Freifeld, B. (2017). 4D surface seismic tracks small supercritical CO_2 injection into the subsurface: CO2CRC Otway Project. *International Journal of Greenhouse Gas Control*, 63, 150– 157.

Pride, S. R. (2005). Relationship between seismic and hydrological properties. In Y. Rubin, & S. S. Hubbard (Eds.), *Hydrogeophysics* pp. 253–290). Dordrecht: Springer.

Pride, S. R., Berryman, J. G., & Harris, J. M. (2004). Seismic attenuation due to wave induced flow. *Journal of Geophysical Research*, 109, 1– 19. https://doi.org/10.1029/2003JB002639

Rickett, J., Duranti, L., Hudson, T., Regel, B., & Hodgson, N. (2007). 4D time strain and the seismic signature of geomechanical compaction at Genesis. *The Leading Edge*, 26, 644– 647. https://doi.org/10.1190/1.2737103

Ringrose, P. S., Mathieson, A. S., Wright, I. W., Selama, F., Hansen, O., Bissell, R., Saoula, N., & Midgley, J. (2013). The In Salah CO2 storage project: Lessons learned and knowledge transfer. *Energy Procedia*, 37, 6226– 6236.

Silvester, J. R. (2000). Determinants of block matrices. *The Mathematical Gazette*, 84, 460– 467.

Smith, T. M., Sondergeld, C. H., & Rai, C. S. (2003). Gassmann fluid substitutions: A tutorial. *Geophysics*, 68, 430– 440.

Tuncay, K., & Corapcioglu, M. Y. (1997). Wave propagation in poroelastic media saturated by two fluids. *Journal of Applied Mechanics*, 64, 313– 320.

Vasco, D. W. (2013). On the propagation of a disturbance in a heterogeneous porous medium saturated with three fluid phases. *Geophysics*, 78, L1– L26. https://doi.org/10.1190/GEO2012-0160.1

Vasco, D. W., Bissell, R. C., Bohloli, B., Daley, T. M., Ferrerri, A., Foxall, W., Goertz-Allmann, B. P., Korneev, V., Morris, J. P., Oye, V., Ramirez, A., Rinaldi, A. P., Rucci, A., Rutqvist, J., White, J., & Zhang, R. (2018). Monitoring and modeling caprock integrity at the In Salah carbon dioxide storage site, Algeria. In S. Vialle, J. Ajo-Franklin, & J. W. Carey (Eds.), *Geological Carbon Storage: Subsurface Seals and Caprock Integrity* pp. 243– 270). Washington, D. C: American Geophysical Union.

Vasco, D. W., Daley, T. M., & Bakulin, A. (2014). Utilizing the onset of time-lapse changes: A robust basis for reservoir monitoring and characterization. *Geophysical Journal International*, 197, 542– 556. https://doi.org/10.1093/gji/ggt526

Vasco, D. W., & Datta-Gupta, A. (2016). *Subsurface fluid flow and imaging*. Cambridge: Cambridge University Press.

Vasco, D. W., Datta-Gupta, A., Behrens, R., Condon, P., & Rickett, J. (2004). Seismic imaging of reservoir flow properties: Time-lapse amplitude changes. *Geophysics*, 69, P1425– P1442. https://doi.org/10.1190/1.1836817

Wang, H. F. (2000). *Theory of Linear Poroelasticity*. Princeton: Princeton University Press.

Wang, Z, Cates, M. E., & Langan, R. T. (1998). Seismic monitoring of a CO_2 flood in a carbonate reservoir: A rock physics study. *Geophysics*, 63, 1604–1617.

Weaver, L., & Anderson, K. (1966). Cranfield field, Cranfield unit, Basal Tuscaloosa Reservoir, Adams and Franklin counties, Mississippi, Oil Recovery from gas-cap Reservoir and Engineering Evaluation of Conserv. Practics in six Reservoirs. Interstate Oil Compact Communication ,Oklahoma City, 42–58.

Whitcombe, D. N., Paramo, P., Philip, N., Toomey, A., Redshaw, T., & Linn, S. (2010). The correlated leakage method—Its application to better quantify timing shifts on 4D data. In *72nd EAGE Conference and Exhibition*, Barcelona, Spain, pp. B037. 14-17 June.

White, J. E. (1975). Computed seismic speeds and attenuation in rocks with partial gas saturation. *Geophysics*, 40, 224– 232.

White, D. J. (2013a). Toward quantitative CO_2 storage estimates from time-lapse 3D seismic travel times: An example from the IEA GHG Weyburn-Midale CO_2 monitoring and storage project. *International Journal of Greenhouse Gas Control*, 16S, S95– S102.

White, D. J. (2013b). Seismic characterization and time-lapse imaging during seven years of CO_2 flood in the Weyburn field, Saskatchewan, Canada. *International Journal of Greenhouse Gas Control*, 16S, S78– S94.

White, D. J., Meadows, M., Cole, S., Ramirez, A., Hao, Y., Carle, S., Duxbury, A., Samson, C., Kendall, J. M., Verdon, J. P., Dietiker, B., Johnson, J., & Morozov, I. (2011). Geophysical monitoring of the Weyburn CO_2 flood: Results during 10 years of injection. *Energy Procedia*, 4, 3628– 3635.

White, D. J., Roach, L. A. N., & Roberts, B. (2015). Time-lapse performance of a sparse permanent array: Experience from the Aquistore CO_2 storage site. *Geophysics*, 80, WA35– WA48.

Wiener, O. (1910). Zur theorie der refraktionskonstanten. *Berichteuber Verhandlungen Koniglich-Sachsischen Gesellschaft Wisseschaften Leipzig*, 62, 256– 277.

Zhang, Q., & Du, B. (2016). *Multiscale and iterative refinement optical flow (MSIROF) for seismic image registration and gather flattening using multidimensional shifts*, pp. 5468– 5472. Texas: Annual Meeting Society of Exploration Geophysicists. https://doi.org/10.1190/segam2016-13954927.1

Zhang, R., Ghosh, R., Sen, M. K., & Srinivasan, S. (2013a). Time-lapse surface seismic inversion with thin bed resolution for monitoring CO_2 sequestration: A case study from Cranfield, Mississippi. *International Journal of Greenhouse Gas Control*, 18, 430– 438.

Zhang, R., Sen, M. K., & Srinivasan, S. (2014). Time-lapse pre-stack seismic inversion with thin bed resolution for CO_2 sequestration from Cranfield, Mississippi. *International Journal of Greenhouse Gas Control*, 20, 223– 229.

Zhang, R., Song, X., Fomel, S., Sen, M. K., & Srinivasan, S. (2013b). Time-lapse seismic data registration and inversion for CO_2 sequestration study at Cranfield. *Geophysics*, 78, B329– B338. https://doi.org/10.1190/geo2012-0386.1

Zhang, R., Vasco, D. W., Daley, T. M., & Harbert, W. (2015). Characterization of a fracture zone using attributes at the In Salah CO_2 storage project. *Interpretation*, 3, SM37– SM46. https://doi.org/10.1190/INT-2014-0141.1